PHOTONICS Research

Do different kinds of photon-pair sources have the same indistinguishability in quantum silicon photonics?

Jong-Moo Lee,[1,*] Alessio Baldazzi,[2] Matteo Sanna,[2] Stefano Azzini,[2] Joon Tae Ahn,[1] Myung-Lae Lee,[1] Youngik Sohn,[3] and Lorenzo Pavesi[2]

[1]Electronics and Telecommunications Research Institute (ETRI), Daejeon 34129, Republic of Korea
[2]Department of Physics, University of Trento, 38123 Trento, Italy
[3]Korea Advanced Institute of Science and Technology (KAIST), Daejeon 34141, Republic of Korea
*Corresponding author: jongmool@etri.re.kr

Received 16 March 2023; revised 4 July 2023; accepted 18 August 2023; posted 21 August 2023 (Doc. ID 489869); published 16 October 2023

In the same silicon photonic integrated circuit, we compare two types of integrated degenerate photon-pair sources (microring resonators and waveguides) using Hong–Ou–Mandel (HOM) interference experiments. Two nominally identical microring resonators are coupled to two nominally identical waveguides, which form the arms of a Mach–Zehnder interferometer. This is pumped by two lasers at two different wavelengths to generate, by spontaneous four-wave mixing, degenerate photon pairs. In particular, the microring resonators can be thermally tuned in or out of resonance with the pump wavelengths, thus choosing either the microring resonators or the waveguides as photon-pair sources, respectively. In this way, an on-chip HOM visibility of 94% with microring resonators and 99% with straight waveguides is measured upon filtering. We compare our experimental results with theoretical simulations of the joint spectral intensity and the purity of the degenerate photon pairs. We verify that the visibility is connected to the sources' indistinguishability, which can be quantified by the overlap between the joint spectral amplitudes (JSA) of the photon pairs generated by the two sources. We estimate a JSA overlap of 98% with waveguides and 89% with microring resonators.

https://doi.org/10.1364/PRJ.489869

1. INTRODUCTION

In quantum computing, it is important to distinguish between physical and logical qubits. The first is the two-level physical systems that are processed in the quantum hardware, while the second is the clusters of redundant physical qubits which store the information [1–5]. On photonic platforms, the number of physical qubits is typically associated with the number of photons whose quality is intrinsically quantified by the purity of the photon states and extrinsically quanitified by their indistinguishability [6,7]. The demand for reliable physical qubits translates into engineering high-quality sources of photons. Currently, there are two main types of integrated sources: deterministic and probabilistic. In the case of deterministic sources, the integration in a silicon photonic-integrated circuit (SiPIC) is still very demanding because of the high coupling loss and the complex fabrication process. On the other hand, there have been many reports of probabilistic photon-pair sources integrated in SiPIC over the last 10 years [8,9]. Then, the correlation between the photons is exploited to produce single photon sources through the heralding mechanism, where one photon of the pair is detected to herald the presence of its twin photon [10]. In the case of deterministic sources, the quality of a generated single photon state is quantified by how close to zero the second-order coherence function $g^{(2)}(0)$ is or, in the case of probabilistic ones, how close to zero the heralded second-order coherence function $g_h^{(2)}(0)$ is.

In this paper, we aim to address the following question: what type of source performs better among the probabilistic sources? This is not a trivial question. The limited amount of physical qubits in the so-called noisy intermediate scale quantum (NISQ) computing era prevents the use of error-correction techniques in universal quantum computing hardware and brings in people to work with quantum simulators, i.e., devices that perform non-universal and problem-focused algorithms [11,12]. Therefore, the most suitable source of photons should be determined by the requirements of the specific implemented algorithm. The ideal short-term aim would be the realization of a sources' library, which can be consulted as needed and updated with the improvements of the sources present in the list.

Among probabilistic sources, the nonlinearity of the photonic material is typically used to create pairs of photons

through nonlinear spontaneous parametric processes. Once the generation is achieved, the generated photons are led to reconfigurable networks of Mach–Zehnder interferometers (MZIs) to produce interference patterns. These are used to qualify the quality of the generated photons [10]. Photon-pair generation and interference between the photons within a SiPIC have gained more and more attention with the growing anticipation toward using a fault-tolerant quantum computer based on linear optical quantum computation [13–17]. In silicon photonics, photon pairs can be generated by spontaneous four-wave mixing (SFWM) in a long waveguide [18,19] or a compact microring resonator [20,21]. Quantum interference of photons in a SiPIC has been demonstrated using heralded photons from non-degenerate photon pairs [20,21] or using degenerate photon pairs composed of two photons that are hard to distinguish from each other [18]. The photon pairs that degenerate in the signal-idler energies can be generated by pumping the SFWM process with two laser wavelengths in, for example, spiraled waveguides, which form the arms of an integrated MZI. The propagation path of the photons can be controlled by adjusting the phase of the MZI, and on-chip quantum interference such as the Hong–Ou–Mandel (HOM) effect can be observed [18,22]. On the other hand, using integrated microring resonators as photon-pair sources, the HOM effect [23–25] of the heralded photons has also been reported more recently [20,21], and a degenerate photon-pair generation from a single microring resonator has been demonstrated [26]. However, on-chip quantum interference of degenerate photon pairs from two microring resonators has not yet been shown and neither has its direct comparison with an experiment using waveguide spirals.

Here, we aim at comparing probabilistic degenerate photon-pair sources made of microring resonators or waveguides. In order to make a fair comparison, we used sources integrated in the same SiPIC. By using microring resonators coupled to waveguides that form the arms of an MZI, we measure the on-chip HOM interference to assess the quality of the generated photon pairs. Microring resonators can be thermally tuned in or out of resonance with the pump wavelengths, to turn on and off the microring-based photon sources, respectively. In this way, we can directly compare the on-chip interference of the degenerate photon pairs from the microrings with respect to the one from the waveguides. Our configuration, composed of the degenerate SFWM with two sources put in parallel inside an MZI, allows us to have a configuration not limited by the purity of the sources but by the indistinguishability of the sources.

The paper is organized in this way. In Section 2, we describe the fabricated devices and the experimental setups used. Section 3 reports the measurement results for the photon-pair sources. Section 4 shows the results of the quantum interference experiments for waveguide-based sources. In Section 5, the results of the quantum interference experiments on waveguide- and microring-resonator-based photon-pair sources in the same integrated photonic circuit are presented. Section 6 discusses the characteristic parameters for the different types of photon-pair sources by using both experimental data and simulations. Section 7 makes a final statement about the main results of this paper. Finally, the Appendix A details the theoretical analysis and the numerical calculations.

2. QUANTUM SILICON PICS AND EXPERIMENTAL SETUPS

The generation of photon pairs in a SiPIC can be achieved through SFWM processes in a low-squeezing regime [27–30]. Typically, two pump photons (at wavelengths λ_{P1} and λ_{P2}) are converted into two newly generated idler and signal photons (at wavelengths λ_i and λ_s) [10]. Non-degenerate SFWM is achieved when identical pump photon wavelengths ($\lambda_{P1} = \lambda_{P2}$) are used so that the generated photons have different wavelengths [31–34], while in degenerate SFWM the situation is inverted, i.e., different pump photon wavelengths ($\lambda_{P1} \neq \lambda_{P2}$) and equal generated photon wavelengths $[\lambda_i = \lambda_s = 2(\lambda_{P1}^{-1} + \lambda_{P2}^{-1})^{-1}]$ [35]. In both cases, the state of the output photons is generally in a squeezed state: the two-mode squeezed state for the non-degenerate case and the single-mode squeezed state for the degenerate one [36,37]. Both states have useful properties for quantum applications. For example, the non-degenerate case is used in combination with the heralding procedure to obtain probabilistic single photon sources, while the degenerate case produces a couple of correlated identical single photons. In this work, the latter case has been implemented in a SiPIC, where the generated pairs of degenerate photons are used to obtain HOM interference.

Two SiPICs are used in this work. Figures 1 and 2 show the schematic diagrams of the integrated circuits for the two devices named SiPIC-1 and SiPIC-2, respectively. Pictures of the actual chips together with their packaging modules are shown in Figs. 1(d) and 2(b). The devices are packaged on a metal-based printed-circuit board (MPCB) with 24-port electrical wiring, and they are pig-tailed to a 24-channel fiber array. The MPCB is in contact with a thermo-electric cooler (TEC) to control the chip temperature. SiPIC-1 and SiPIC-2 are based on silicon waveguides with a nominal 450 nm × 220 nm cross section (typically 480 nm × 210 nm after fabrication) and were fabricated with IMEC/Europractice using their passive+ silicon-on-insulator (SOI) platform, similar to our previous report [22]. Dispersion tailoring was not used to optimize SFWM processes since previous experiments [19] show a quite broad generation spectrum for photon pairs in silicon waveguides. The measured waveguide propagation loss is 2 dB/cm, a relevant feature for the sources we want to compare. For microring resonators, this determines the quality of the cavity, whose design has the coupler parameters adjusted to the losses. For waveguide spirals, it gives an effective length of $L_{\text{eff}} = [1 - \exp(-\alpha L)]/\alpha$, with L being the geometrical length and α being the propagation loss per unit of the length, which enters quadratically in the SFWM generation rate [38]. From the analysis of this quantity, we choose the geometrical length of the long spirals in SiPIC-1 and SiPIC-2, finding 1.5 cm as an optimal value.

Figure 1 (top) shows the schematic experimental setup based on SiPIC-1. Two continuous-wave (CW) tunable laser diodes (CoBrite from IDPhotonics) at $\lambda_{P1} = 1544.08$ nm and $\lambda_{P2} = 1556.18$ nm are combined by a 3-dB fiber-optic coupler and provide the pump photons. The combined beam is passed through an optical notch filter (NF) [19,22] to eliminate

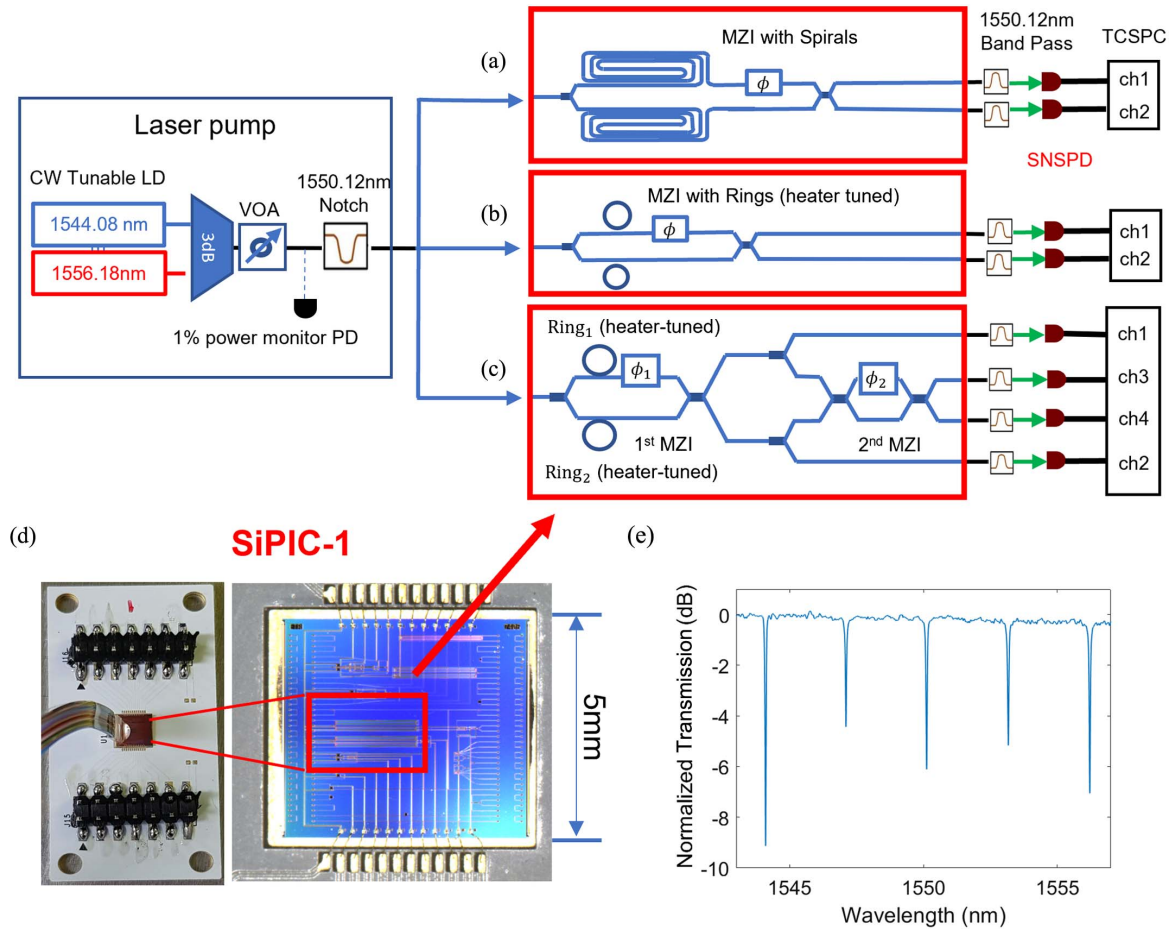

Fig. 1. (top) Experimental set-up to measure photon-pair generation and multi-source quantum interference in SiPIC-1. The blue rectangle contains the pump laser's apparatus. The thick blue lines with arrows represent the fibers coupling the pump beams to the SiPIC, which is represented by the different circuits enclosed by the red rectangles. The circuit in (a) represents the photon-pair sources based on spiral waveguides that form the two arms of an MZI. The circuit in (b) represents the photon-pair sources formed by the microrings. The circuit in (c) represents the composite photon-pair sources based on both waveguides and microrings. These are followed by a second MZI to measure the quantum interference of the generated photons. On the right, the detection channels (ch 1–ch 4) are represented. These are based on a sequence of optical fibers, band-pass filters, superconductor nanowire single photon detectors (SNSPDs), and a time-correlated single photon counting module interfaced to a computer for further processing. (d) On the left is the photograph of the packaged SiPIC-1 chip. On the right is the zoomed-in image of the chip with the circuit highlighted by the red rectangle. (e) The normalized transmission spectrum of the circuit in (b) when the two microring resonators are tuned in resonance with the pump photons wavelengths.

photon noise within a 1.6 nm bandwidth around $\lambda_i = \lambda_s = 1550.12$ nm, which is the wavelength of the on-chip generated photon pairs. Then, the pump photons are inserted into the selected input fiber of the fiber array, which is coupled to the chip by grating couplers and whose coupling loss is measured to be 4.2 dB. In SiPIC-1, different circuits are presented [Figs. 1(a)–1(c)]. These are based on MZIs with two nominally identical photon-pair sources located in their arms. The photon-pair sources are based on 15-mm-long waveguide spirals [Fig. 1(a)] or on 30-μm-radius microring resonators [Figs. 1(b) and 1(c)]. The microrings are coupled to micro-heaters (metal wires on top of the microring), which allow thermal tuning of their resonances.

Figure 1(e) shows the normalized transmission spectrum of one of the microrings taken by scanning the wavelength of one of the tunable laser diodes. Transmission resonances are observed at 1544.08 nm, 1550.12 nm, and 1556.18 nm, i.e., at the wavelengths of the pump photons and of the generated photon pairs. Their free spectral range (FSR) is about 3 nm, and their loaded quality factor (Q-factor) is about 1.5×10^4. Micro-heaters are also integrated on one arm of the MZI to act as phase shifters (ϕ) in order to compensate for unwanted phase differences between the two arms. The efficiency of the micro-heater (0.6 μm × 40 μm) of the MZI is measured to be about 25 mW/π with an overall resistance of about 50 Ω. The efficiency of the heater is relatively poor with respect to our previous report of 12 mW/π [39], and this is mainly due to the additional power consumption along the wires from the micro-heater to the bonding pad, which adds to the power dissipated at the contact resistance between the metal wire and the heater layers. We expect that the heating efficiency can be improved simply by increasing the length of the heater.

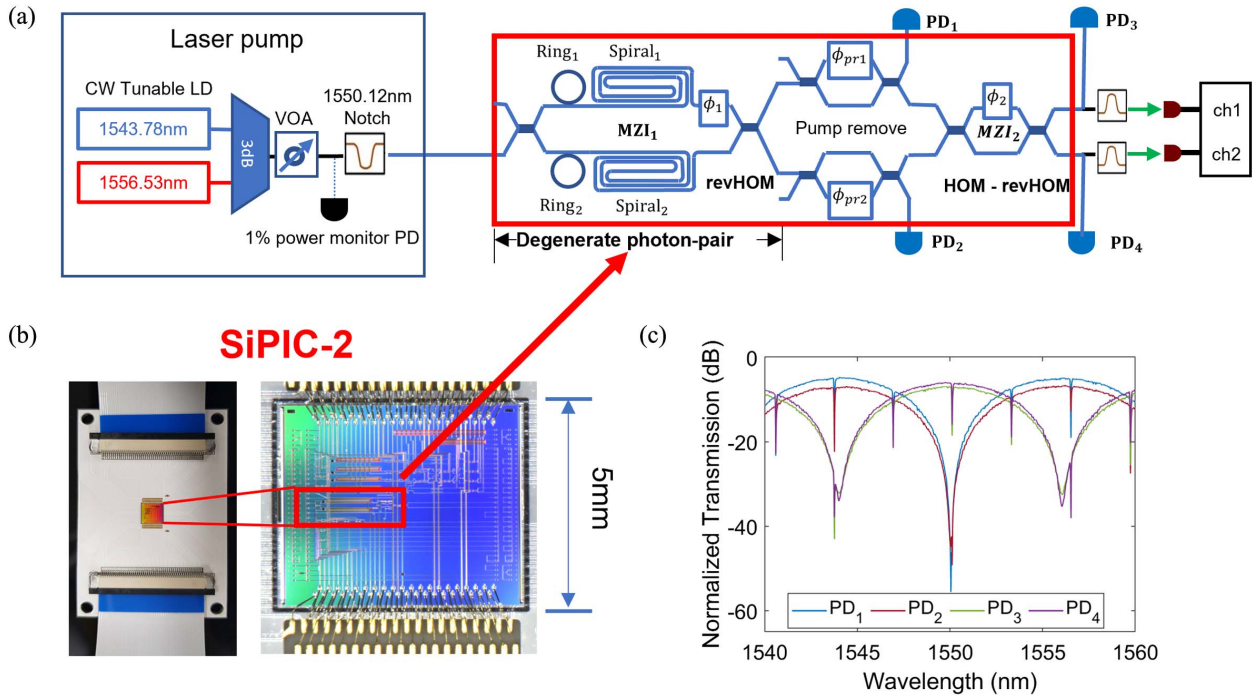

Fig. 2. Experimental set-up to measure photon-pair generation and multi-source quantum interference in SiPIC-2. The blue rectangle contains the pump laser's apparatus. The red rectangle contains a scheme of the SiPIC. Four photodiodes (PD_1–PD_4) are interfaced to the output of SiPIC-2 by optical fibers and grating couplers. In addition, two single photon counting channels (formed by the same sequence as in Fig. 1) are used to measure the output coincidence counts. (b) On the left is the photograph of the packaged SiPIC-2 chip. On the right is the zoomed-in image of the chip with the circuit highlighted by the red rectangle. (c) The normalized transmission spectra measured by the different photodiodes (blue line PD_1, red line PD_2, green line PD_3, and violet line PD_4) while scanning the wavelength of one of the tunable laser diodes.

In the circuit reported in Fig. 1(c) the length of the waveguide in the MZI arms is 240 μm. This implies that photon pairs can also be generated in the waveguide of the MZI of Fig. 1(c). In order to isolate the waveguide contribution, we thermally tuned the microring out of resonance with respect to the pump photons (labeled RingOff). We changed the temperature of the microrings from 11.7°C ± 0.1°C (RingOn, microring resonant with the pump photons) to 20°C ± 0.1°C (RingOff) since the microring resonance wavelength temperature dependence is 80 pm/°C [39]. The circuit shown in Fig. 1(c) includes an additional second MZI. The first MZI, similar to the circuits shown in Figs. 1(a) and 1(b), contains the degenerate photon-pair sources and a phase shifter (ϕ_1), while the second MZI measures the quantum interference of the generated photon pairs. Note that the two multi-mode interference devices (1 × 2 MMIs) are used after the first MZI to tap and monitor the generated photons. The second MZI also includes a phase-shifter (ϕ_2). This is placed 740 μm away from the microrings to avoid any thermal cross talk. At the output of the SiPIC, the photons are out-coupled through gratings using the fiber arrays, filtered off the pump photons with band-pass filters (BPFs, with a 0.8 nm bandwidth centered at 1550.12 nm), and detected by using super-conducting-nanowire single-photon detectors (SNSPDs, EOS from Single Quantum) [19,22]. Then, the SNSPD single-photon events are counted by a time-correlated single photon counter (TCSPC, Logic16 from UQdevices) and analyzed by logical post-selection.

Figure 2(a) shows the schematic experimental setup based on SiPIC-2. With respect to the circuit shown in Fig. 1(c), this is an improvement. It is aimed at a direct comparison between microring and waveguide sources by integrating both an HOM and a reverse HOM experimental set-up with a scheme similar to the one shown in Fig. 1(c). In SiPIC-2, the microrings have 28.5-μm-long radii, the spiral waveguides are 15-mm-long, and the grating couplers have a measured coupling efficiency of 3.3 dB. In addition, SiPIC-2 includes photon pump filters realized by asymmetric MZIs (a-MZIs) and placed after the sources to reduce the accidental coincidence (noisy) counts. The asymmetric length of the a-MZI is designed to be 47.2 μm, which yields a 12.8 nm (1600 GHz) FSR to match four times the nominal FSR of the microrings. Figure 2(c) shows the normalized transmission spectra measured with the photodiodes (PD_1–PD_4) visible in Fig. 2(a). PD_1 and PD_2 measure the pump filter characteristics, while PD_3 and PD_4 measure the transmitted photons. After tuning the resonance of the microring close to the pumping wavelengths (1543.78 nm and 1556.53 nm) and tuning the pump filter MZIs to reject the pump, the following data are observed: a loaded Q-factor of 3×10^4 (twice larger than the Q-factor of the microrings in SiPIC-1), an FSR of 3.2 nm (400 GHz, similar to the design value), a pump filter FSR of 12 nm (1500 GHz), and a pump rejection ratio larger than 30 dB. This last value is large enough to significantly reduce the accidental counts due to the pump photons in the coincidence measurements.

3. PHOTON-PAIR GENERATION AND HERALDED SINGLE PHOTONS FROM MICRORING RESONATORS AND WAVEGUIDE SPIRALS

The overall quality of the integrated sources has been characterized by the measurements of the coincidence-to-accidental ratio (CAR) [19], the heralding rate [19,22], and the $g^{(2)}(0)$ of the heralded photons or $g_h^{(2)}(0)$ [10]. To measure the $g_h^{(2)}(0)$, we added a 3 dB fiber splitter between the SiPIC-1 outputs and the SNSPDs to realize a Hanbury–Brown–Twiss interferometer [10].

Figure 3(a) shows the measured CAR and heralding rate and Fig. 3(b) the measured $g^{(2)}(0)$ of the heralded photons from the spiral waveguide sources [Fig. 1(a), in short spirals in the following] and from the microring resonator sources [Fig. 1(b), in short rings in the following] in SiPIC-1. The heralding rate for a microring resonator is 5 kHz for 1 mW pump power (−119 dB conversion efficiency for heralding), while the heralding rate for a spiral waveguide is 10 kHz for 5 mW pump power (−124 dB conversion efficiency for heralding). The coincidence time window of the TCSPC was set equal to 0.2 ns. Measurements show that the spirals have a larger CAR but a smaller heralding rate than the rings at high pump powers. This last indicates that the field enhancement factor in our microring resonators is high enough to compensate for the length of the spirals. In addition, we observe in Fig. 3(b) high-quality heralded single photons at low pump powers [vanishing $g_h^{(2)}(0)$], while multi-photon contributions become relevant at high pump powers (above 2 mW). The multi-photon contribution appears to be more severe for photon pairs generated from the rings than from the spirals.

The circuit in Fig. 1(c) allows for tuning the rings in resonance (RingOn) and out of resonance (RingOff) with λ_{p1} and λ_{p2} and observing the photon-pair generations at the output channels ch 1 and ch 2. Figure 4 shows the CAR, the heralding rate, and the $g_h^{(2)}(0)$ for the RingOn and RingOff configurations. Figure 4(a) shows that the heralding rate is larger for the RingOn configuration than for the RingOff configuration. The result for the RingOn configuration is similar to what is shown in Fig. 3(a) for the ring, while the CAR and the heralding rate for the RingOff configuration are lower than those reported for the spirals in Fig. 3(a), which is due to the difference in the waveguide lengths (240 μm versus 15 mm) that enters quadratically in the photon-pair generation rate. To measure $g_h^{(2)}(0)$, we set the two rings in the two arms of the first MZI in the RingOn and the RingOff modes, respectively, while we set

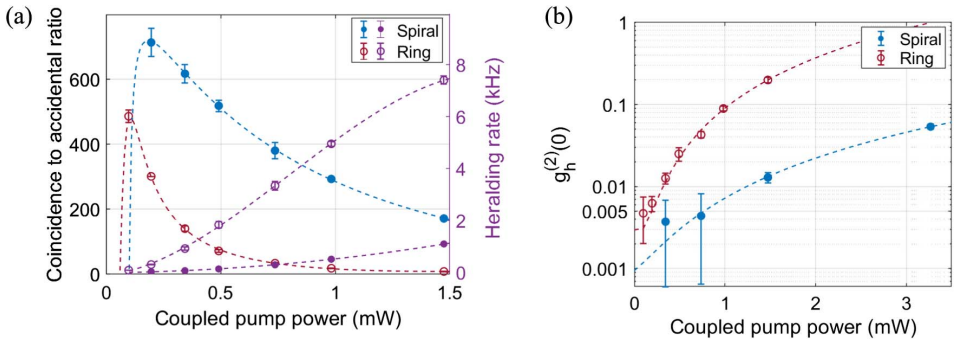

Fig. 3. Measurement results of the characteristics of the photon-pair sources in the circuits shown in spirals [Fig. 1(a)] and rings [Fig. 1(b)]. (a) Coincidence to accidental ratio as a function of the pump power coupled to the chip (blue dots refer to the spirals, empty red dots to the rings), and heralding rate as a function of the coupled pump power (violet dots refer to spirals, empty violet dots to microrings). (b) $g_h^{(2)}(0)$ as a function of the coupled pump power (blue dots refer to spirals, empty red dots to microrings).

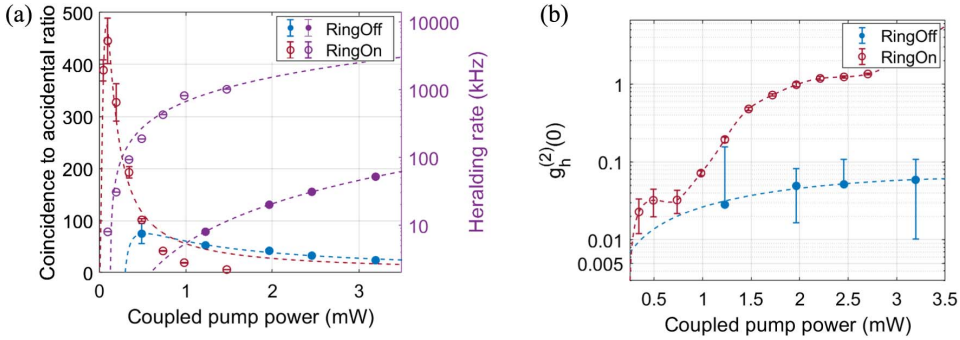

Fig. 4. Measurements of the characteristics of the photon-pair sources in the circuit shown in Fig. 1(c). (a) The coincidence to the accidental ratio as a function of the pump power coupled to the chip (blue dots refer to the RingOff mode, i.e., the microrings are off-resonant with the pump photons wavelengths; the empty red dots refer to the RingOn mode, and the microrings are resonant with the pump photons wavelengths), and heralding rate as a function of the coupled pump power (violet dots refer to RingOff, empty violet dots to RingOn). (b) $g_h^{(2)}(0)$ as a function of the coupled pump power (blue dots refer to RingOff, empty red dots to RingOn).

$\phi_2 = \pi$ of the second MZI. In this way, we can herald by ch 2 detections the single photons at ch 1 or ch 3, i.e., by post-selection we measure the coincidences of ch 1 and ch 3 heralded by ch 2 to get $g_h^{(2)}(0)$ [Fig. 4(b)]. The results are similar to what can be observed in Fig. 3(b) when the different waveguide lengths or microrings are considered.

Data for SiPIC-2 are shown in Fig. 5. During the measurements, the phase ϕ_2 of the second MZI is fixed at zero [see Fig. 2(a)] and, also in this case, the two modes RingOn and RingOff are possible. When the RingOn mode is selected, the rings are effective as photon-pair sources, while in the RingOff mode the spirals are effective. The CAR is larger than 1000 for the spirals (600 for the rings), which demonstrates the effect of the removal of the pump photons by the on-chip pump filters based on the a-MZIs, as in our previous report [19]. However, the heralding rate for the rings is relatively low due to the additional 3 dB losses caused by the 15-mm-long spirals, which follow the microrings on the arms of the first MZI (a decrease of the coincidence probability by $1/2 \times 1/2 = 1/4$ is estimated) and is due to large two-photon absorption (TPA) losses in the microring because of the high Q-factor.

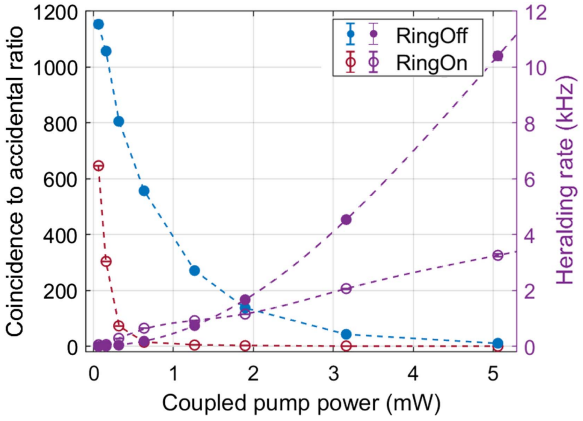

Fig. 5. Measurements of the characteristics of the photon-pair sources in SiPIC-2. The coincidence to the accidental ratio as a function of the pump power coupled to the chip (blue dots refer to the RingOff mode, i.e., the microrings are off-resonant with the pump photons wavelengths; empty red dots refer to the RingOn mode, i.e., the microrings are resonant with the pump photons wavelengths), and the heralding rate as a function of the coupled pump power (violet dots refer to RingOff, empty violet dots to RingOn).

Regarding TPA, we observe that Figs. 3(a), 4(a), and 5 show a saturation of the quadratic behavior of the heralding rate with respect to the pump power. However, as the following sections show, our comparative experiments are run by using low pump powers to achieve optimal values of CAR and $g_h^{(2)}(0)$, where the quadratic behavior of the generation rate is observable. This sets us in a regime where TPA is not limiting the performances. Indeed, using low pump powers, the conversion efficiency of photon-pair generation is low but nonlinear losses given by TPA and free carrier absorption can be neglected with respect to linear scattering loss [40]. Thus, we can affirm that SFWM in SiPIC-1 and SiPIC-2, and especially for rings, should exclusively be performed at low optical pump powers to avoid a steep roll-off in performance at higher powers [41].

4. REVERSE HONG–OU–MANDEL INTERFERENCE FROM WAVEGUIDE SPIRALS

To prove the indistinguishability of the photons generated by the two sources, we performed quantum interference measurements with SiPIC-1 [18]. First, we studied the 15-mm-long spiral-waveguide-based sources in the circuit of Fig. 1(a), and we measured the dependence of the coincidence rates between ch 1 and ch 2 as a function of the phase ϕ of the MZI at a fixed pump power of 1.5 mW (CAR = 170). Figure 6 compares the measured counts detected at the two output channels of the MZI in Fig. 6(a), showing the classical light transmission with the coincidence rates between the two channels in Fig. 6(b) and showing the quantum interference between the generated photons. As expected by the theoretical analysis reported in the Appendix A or in Refs. [18,22], the coincidence rates follow $\sin^2(\phi - \frac{\pi}{2}) = \cos^2(\phi)$, while the classical light transmission follow $\sin^2[(\phi - \frac{\pi}{2})/2]$ or $\cos^2[(\phi - \frac{\pi}{2})/2]$. Some deviations with respect to the theory are observed due to the use of a first 1×2 MMI instead of a 2×2 MMI in the MZI. The coincidence measurement result is due to a reverse HOM quantum interference of degenerate photon pairs at the second MMI of the MZI, and its high visibility of 98.8% demonstrates the indistinguishability of the photon pairs generated by the two spirals [10,18]. We use the following formula for the visibility (V): $V = \frac{R_c^{\max} - R_c^{\min}}{R_c^{\max}}$, where $R_c^{\max}$ and $R_c^{\min}$ are the maximum and

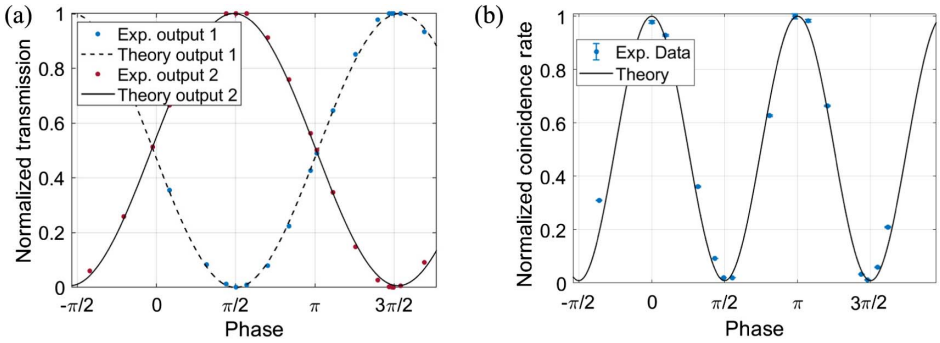

Fig. 6. (a) Measured classical transmissions from the two outputs (blue dots ch1, red dots ch2) of the MZI in Fig. 1(a) (SiPIC-1) as a function of the phase ϕ compared to the theory (dashed line ch1, continuous line ch2). (b) Measured (blue dots) and theoretical (line) coincidence rates between the two outputs of the MZI as a function of the phase ϕ.

minimum coincidence rates, respectively. In the Appendix A, such formulas are expressed in terms of coincidence probabilities in Eqs. (A29) and (A40). Then, we used the rings in the circuit of Fig. 1(b). However, because the micro heater of the phase shifter in the MZI is located too close (130 μm) to the microring, a large thermal cross talk caused the microring resonance to shift out of resonance from the pump wavelength when the phase ϕ was varied. This impeded the measurement.

5. ON-CHIP DIRECT COMPARISON OF MICRORING RESONATORS AND WAVEGUIDE SPIRALS

The circuits of SiPIC-1 in Fig. 1(c) and of SiPIC-2 in Fig. 2(a) allow comparing the quantum interference of photon pairs produced by microring resonators or waveguides. Photons are generated in the first MZI, while quantum interference measurements are performed by changing the phase ϕ_2 of the second MZI. Actually, this corresponds to a complex HOM measurement sequence [a reverse HOM in the first MZI and a sequence of an HOM and a reverse HOM in the second MZI, see in particular Fig. 2(a)].

Let us first consider SiPIC-1. Given the CAR and $g_b^{(2)}(0)$ values measured for the two RingOn and RingOff configurations (Fig. 4), the pump power was set to 1 mW for RingOn (CAR = 19, equivalent to 5% of accidental counts) and to 3.2 mW for RingOff (CAR = 24, equivalent to 4% of accidental counts). Figure 7(a) shows the measured classical-light transmissions from channel 1 (ch 3 detector) and channel 2 (ch 4 detector) of the second MZI as a function of ϕ_2. Figures 7(b) and 7(c) show the measured coincidence rates between channel 1 and channel 2 as a function of ϕ_2 in the RingOn and RingOff configurations, which correspond to the quantum interference of photons generated in rings and in spirals, respectively. Note that to compensate for slight variations in the photon-pair generation rate due to the thermal cross talk (heat flow from the micro-heater on the phase shifter in the second MZI to the first MZI), we normalized the coincidence rates between ch 3 and ch 4 to the coincidence rates between ch 1 and ch 2 [see Fig. 1(c)].

As expected and discussed in the Appendix A, the classical light transmissions behave as $\cos^2(\phi_2/2)$ or $\sin^2(\phi_2/2)$, while the coincidence rates behave as $\cos^2(\phi_2)$. For the RingOn configuration [Fig. 7(b)], a visibility of 80% is observed, which is lower than the 98.8% visibility measured for the RingOff configuration [Fig. 7(c)]. The visibility for the RingOff configuration is high considering the presence of 4% of accidental coincidences at a CAR = 24. These additional coincidences are due to the classical interference of accidental photons coming from the residual pump, whose interference depends on the phase difference accumulated by the pump photons propagating from the first MZI to the second MZI. Therefore, considering a measured ratio of the ch 3 and ch 4 counts of about 3% for $\phi_2 = \pi/2$ and 52% for $\phi_2 = \pi$ implies that accidental coincidences are reduced at $\phi_2 = \pi/2$, yielding a high HOM visibility for the RingOff configuration as observed in Fig. 7(c).

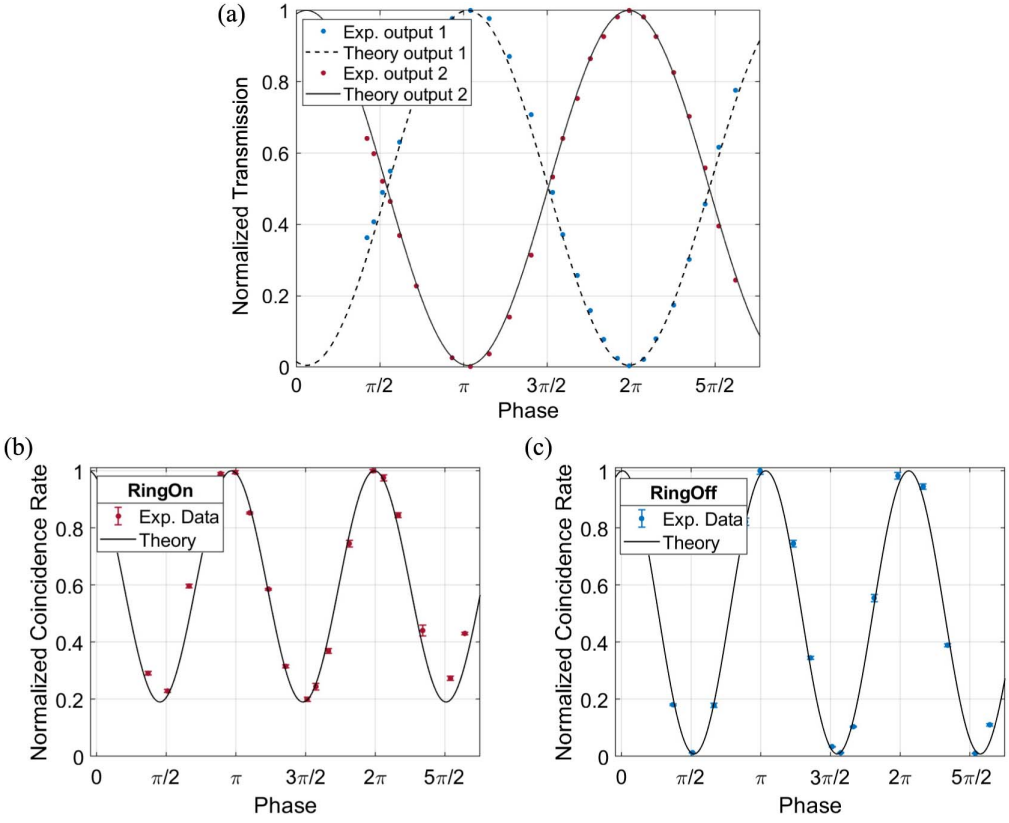

Fig. 7. (a) Classical light transmissions at the outputs of the two channels of the second MZI in the circuit of Fig. 1(c) (SiPIC-1) as a function of the phase ϕ_2 (dots measurements, lines theory). (b) The coincidence rates (red dots experiments, line theory) as a function of ϕ_2 for the RingOn configuration. (c) The coincidence rates (blue dots experiments, line theory) as a function of ϕ_2 for the RingOff configuration.

Figure 8 shows the measured HOM interferences for the SiPIC-2 when the phase ϕ_2 of the second MZI is varied [Fig. 2(a)]. For the RingOn configuration [Fig. 8(a)], an HOM interference visibility of 94% is measured when a pump power of 0.3 mW (corresponding to a CAR = 74 in Fig. 5) is used. The RingOn visibility decreases to 89% for a pump power of 0.6 mW (CAR = 15). Accidental counts impact at 1.3% for a CAR = 74 and 6.3% for a CAR = 15. So the 94% HOM interference visibility is equivalent to a 95.3% visibility when the accidental noise is removed. For the RingOff configuration [Fig. 8(b)], HOM interference visibilities of 99% for 0.6 mW pump power (CAR = 557) and of 91% for a pump power of 5 mW (CAR = 12) are observed. The accidental counts impact at 0.2% for a CAR = 557 and 7.7% for a CAR = 12. So the 99% HOM interference visibility is equivalent to 99.2% visibility when the accidental counts are excluded. Measurements show again that the HOM interference visibility depends on the CAR of the measured photon pairs. In addition, accidental photons due to residual pump classical interference yield a measured ch 1 to ch 2 ratio of 97% for $\phi_2 = 0$ and of 90% for $\phi_2 = \pi/2$, showing the effective role of the pump filters and less relevance of this noise for SiPIC-2 than for SiPIC-1. Finally, the better HOM interference visibilities for SiPIC-2 rather than the HOM interference visibilities for SiPIC-1 are related to the enhanced CAR due to the integrated pump-filters and to an improved fabrication uniformity of the microrings in SiPIC-2 as compared to SiPIC-1.

6. DISCUSSION

The two types of photon-pair sources (waveguides and microring resonators) were simulated taking into account the input pump photon spectra as well as the band-pass filters (BPFs) at the output channels. The joint spectral intensity (JSI) of the generated pairs was calculated, as detailed in Appendix A.1. Figure 9 shows the JSI for the different sources in SiPIC-1 and SiPIC-2 (15-mm-long and 240-μm-long spiral waveguides, and microring resonators with Q-factors 1.5×10^4 and 3×10^4). In particular, it is worth noting that even in a degenerate SFWM process the generated photon pair wavelengths have a dispersion around $\lambda_s \simeq \lambda_i$ due to the spectral width of the pump laser lines and the generation band of the FWM process.

The different shapes of the JSI for the photon pairs generated by the spiral waveguides [Figs. 9(a) and 9(b)] are mainly due to their different lengths. The longer waveguide acts as an additional narrow band-pass filter that modifies the JSI. This modification can be understood from the phase matching function reported in Eq. (A10) and contained in the joint spectral amplitude (JSA), Eq. (A9). It is also evident that the JSI shapes of the waveguides are wider than the shape of the microring resonators. This implies a higher correlation in the generated photons from the waveguides than from the microring resonators. These wide JSIs can be explained by the filtering of the broad waveguide generation band (between the two pump photon wavelengths) by the BPF. Filtering also lowers the photon-pair source brightness. In the case of the microring resonators, the effect of the BPF is negligible because of the narrow resonance spectral widths of the microrings. Moreover, their high Q-factor values make their JSIs narrow and increase their photon-pair generation probabilities, which depend on a cubic law of the Q-factor value [38]. However, high Q-factor values make the microring resonator more sensitive to thermal cross talk and TPA.

Table 1 summarizes the measured and simulated properties of the two types of sources considered in this work. In the simulations for the JSI and purity, the two waveguides/microring resonators are assumed both identical to their nominal design values. This implies that the simulated values are not affected by the small variations of the nominal parameters present in the fabricated structures. The purity has been calculated by using Eq. (A4) and the JSA overlaps have been calculated using the experimental results of the visibility, following the procedure discussed in Appendices A.2 and A.3, and more specifically Eq. (A33).

In Appendix A.4, we discuss how unwanted residual pump noise can be included into the description of the visibility in terms of the JSA overlaps. The qualitative effect consists in lower values of the visibility because of lower values of the signal-to-noise ratio. This behavior is found experimentally in Fig. 8, where we observe different values of visibility for different CAR values using an asymmetric MZI (a-MZI) to filter the residual pump. In Table 1, we report the best values of observed visibility, and the computation of the JSA overlaps

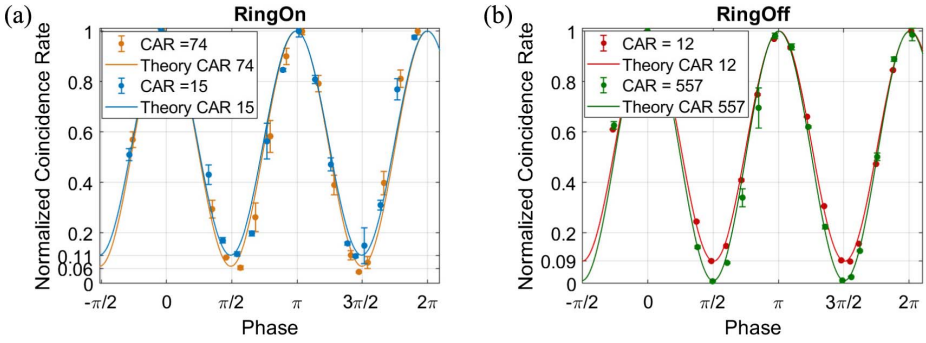

Fig. 8. Coincidence rates between the output channels of the second MZI in the SiPIC-2 device [Fig. 2(a)] as a function of phase ϕ_2 of the second MZI. (a) RingOn configuration for two pump powers (orange 0.3 mW and blue 0.6 mW). Dots are the experimental data, while lines are the theoretical fits. (b) RingOff configuration for two pump powers (green 0.6 mW and red 5 mW). Dots are the experimental data, while lines are the theoretical fits.

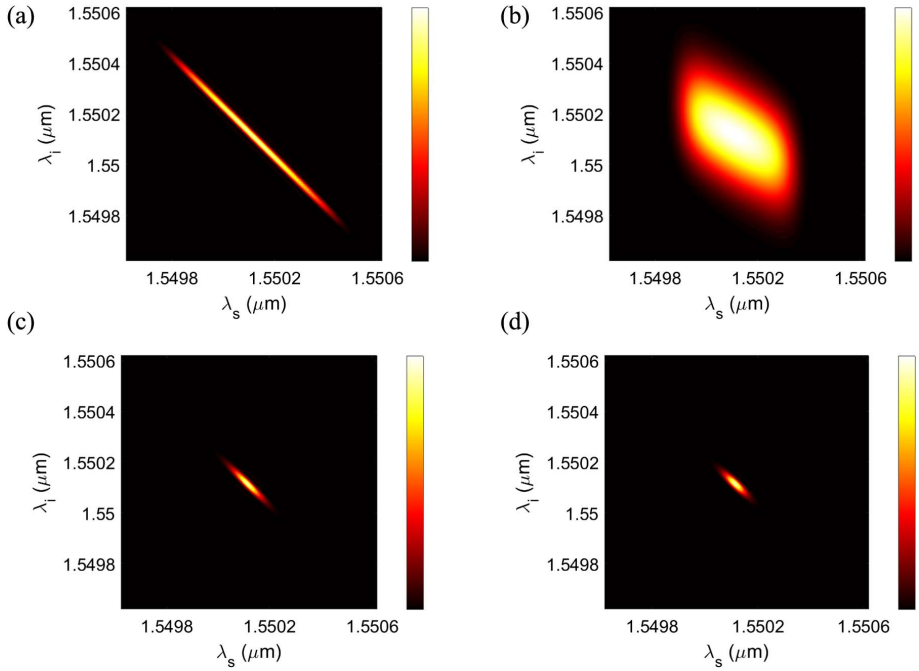

Fig. 9. Simulated JSI as a function of the signal (λ_s) and idler (λ_i) wavelengths after the application of a band pass filter centered at 1550.12 nm with a bandwidth of 100 GHz (0.8 nm) with CW pump lasers for (a) the 15-mm-long waveguide spiral, (b) the 240-μm-long waveguide spiral, (c) the microring resonator with an FSR around 3 nm and a Q-factor 1.5×10^4 (0.1 nm FWHM), and (d) the microring resonator with an FSR around 3.2 nm and a Q-factor 3×10^4 (0.05 nm FWHM). The simulations are based on parameters corresponding to the different circuits in Figs. 1 and 2.

Table 1. Summary of the Relevant Properties of the Photon-Pair Sources in SiPIC-1 and SiPIC-2

	Observed Visibility	Simulated Purity	Computed JSA Overlaps
15-mm waveguides (SiPIC-1)	98.8%	81%	97.6%
Microrings (SiPIC-1)	80%	90%	66.6%
0.24-mm waveguides (SiPIC-1)	98.8%	86%	97.6%
15-mm waveguides (SiPIC-2)	99%	81%	98%
Microrings (SiPIC-2)	94%	90%	88.7%

does not take into account the noise contribution discussed in Appendix A.4. Thus, the reported value of the computed JSA overlaps is a lower bound, since the assumption of negligible noise contribution might not be correct for our experiments.

In the case of the waveguide source, the purity goes from a simulated value of 20% in the unfiltered case to the value reported in Table 1 when a BPF is used. The simplicity in the fabrication of a waveguide source has its bottleneck in the necessity to use a high-quality BPF to produce photons with high spectral purity. Indeed, the results reported in the Table 1 show similar values for the waveguide devices of SiPIC-1 and SiPIC-2 despite that the fabrication of the latter resulted in devices with better performances. Indeed, the features of the microring resonators greatly improved from SiPIC-1 to SiPIC-2 due to a better fabrication uniformity achieved with the second process.

One may wonder why the visibility in the case of the waveguide is larger than the visibility of the microring resonator case, even if the purity shows an opposite trend. This point constitutes one of the main interesting aspects of the experiments described in Sections 4 and 5. In many published experiments the sources are independent [20,21,24], while in our case the two sources are not independent, and therefore the visibility is not linked to the purity of the individual sources. For example, in the case of independent sources, one typically uses non-degenerate SFWM to generate two pairs of idler and signal photons. The wave function is the product of the two pair wave functions, and the heralding procedure is the partial trace with respect to the heralding twins. The visibility is then given by the purity of each heralded photon. For standard microring resonators this means that the visibility cannot exceed 92% [42,43]. Therefore, the property of being independent brings the overall wave function of the state to be separable, while in our case the state is not separable. To verify this, we can consider the state generated by the pair of sources, Eq. (A23) in the Appendix A for small squeezing (the meaning of the different symbols is given in the appendix),

$$|\Psi\rangle_{\mathrm{II}} \sim \int \mathrm{d}\omega_i \mathrm{d}\omega_s [F_1(\omega_i,\omega_s)\hat{a}_1^\dagger(\omega_i)\hat{a}_1^\dagger(\omega_s) + F_2(\omega_i,\omega_s)\hat{a}_2^\dagger(\omega_i)\hat{a}_2^\dagger(\omega_s)]|\mathrm{vac}\rangle, \quad (1)$$

where F_1 and F_2 are the JSAs of the two sources. Crucially, $|\Psi\rangle_{II}$ is a superposition between pairs of photons generated in the two sources. What is generated in our case consists of a photon pair in a superposition of two paths, while in the case of independent sources and non-degenerate FWM, two pairs are generated, and after heralding, a state with one heralded photon in each path is obtained. The Appendix A shows how the visibility is connected to the indistinguishability of the sources, represented by the JSA overlap $\int d\omega_i d\omega_s F_1(\omega_i,\omega_s)\cdot \bar{F}_2(\omega_i,\omega_s)$. In particular, given our definition of observed visibility, the visibility can be written as

$$V=\frac{2\int d\omega_i d\omega_s F_1(\omega_i,\omega_s)\bar{F}_2(\omega_i,\omega_s)}{1+\int d\omega_i d\omega_s F_1(\omega_i,\omega_s)\bar{F}_2(\omega_i,\omega_s)}, \tag{2}$$

which is presented in Eq. (A33) and derived in Appendices A.2 and A.3. Therefore, even if the purity is low, what matters is how much the two sources are indistinguishable. This is quantified by the integral overlap between the JSA of the two sources, and its relation to the visibility is given by Eq. (A33). We note that for $F_1=F_2$ the state generated by the couple of sources is exactly the input state used to perform a reverse HOM experiment [see Eq. (1)], and Eq. (2) gives $V=1$. The result of this visibility proves that there is good matching between the spectral shapes of the photon pair generated by the waveguides in SiPIC-1 and SiPIC-2 and by the microring resonators in SiPIC-2. The microring resonators in SiPIC-1 show a significantly lower JSA overlap and a lower measured visibility. This can be because some geometrical parameters can be slightly different between the two microring resonators. Therefore, the variability in the performances of the microring resonators between the two SiPIC models gives an idea about the higher requirements on the fabrication process needed to reach a high level of uniformity in the components to assure proper indistinguishability of the different integrated sources when microrings are used. We note that the source purity is not affected by the Q-factor of the microring and reaches a theoretical maximum value of 92% [42,43].

We conclude this section by reporting some numerical results obtained by simulating small deviations of one of the two sources with respect to the nominal design values. In the case of the spiral-waveguide-based source, differences with respect to losses, length, and width of the waveguides can be responsible for a lower JSA overlap. These characteristics determine the generation band of the process since they enter into the phase matching function [Eq. (A10)]. Let us note that the BPFs select 100 GHz (50 GHz at 3 dB bandwidth) around 1550.12 nm as it is described by the filters' spectral amplitude in Eq. (A33). The filtering acts as a quantum eraser [44], deleting the information about possible differences in the generation bands and making the structures less sensitive to deviations from nominal values. Thus, we expect that a narrower BPF will result in higher visibility. Given the spectra of our filters, from our simulations we do not observe any significant change in the JSA overlaps by varying the relative width of the waveguides. Indeed, by considering a width variation of 5% with respect to the nominal value, the JSA overlap only decreases to 99.98%. Instead, varying by 10% the effective length L_{eff} of one of the two spiral waveguides with respect to the other, a JSA overlap of 98% is found. Comparing these values with Table 1, we infer that differences in propagation loss and/or length can be responsible for lower values of JSA overlaps. The case of the microring-resonator-based sources is not affected by the action of the filters, and even if their footprint is much smaller, deviations in the coupling coefficients and ring losses can have a big impact on the JSA overlap. In Ref. [45], it has been shown that devices uniformity within 1% is achievable by using advanced processes in the same PIC. In a microring resonator, the coupling gap uniformity plays a very important role [46–48], and it can determine a different coupling regime of the device. As an example, from our numerical simulations based on Eq. (A11), we observe that the JSA overlaps decrease to 82% for a 25% Q-factor deviation and to 67% for a 50% deviation. Figure 12 at the end of the Appendix A shows the simulated JSA overlaps as a function of the variations of L_{eff} for the spiral waveguides and the variations of the Q-factors for the microring resonators. Finally, the outcomes of our numerical analysis support our experimental results, where variations of the nominal design feature have a stronger effect on the microring resonators by decreasing the JSA overlap. Clearly, for both kinds of sources, large variations result in an increase in their distinguishability, allowing an answer to the question "Where did the pair generate?" and suppressing the visibility of the HOM interference. Generally, we expect and observe that in the resonant case the impact of the non-uniformity of the devices is more severe.

7. CONCLUSION

We performed Hong–Ou–Mandel fringe interference experiments of degenerate photon pairs generated on-chip from nominally identical and non-independent probabilistic sources. Non-independency of the sources is achieved by putting them on the two arms of an MZI, while the HOM interference is realized by a second MZI. Through such a configuration, it is possible to simultaneously excite both sources and create a superposition of twin photons from the two sources, which is actually a path-entangled state. The photon-pair sources we studied and compared are microring resonators and waveguides. At best, we measured the on-chip HOM visibility of 94% for microring resonators and 99% for waveguides. The visibility of the HOM interference gives information about the indistinguishability of the twin photons generated, which is in turn the indistinguishability of the two nominally identical sources. Crucially, the non-independency of the degenerate photon-pair sources results in the visibility being limited only by the indistinguishability and not by the purity. As a matter of fact, this places us in an ideal situation to address the question that titles this work, whose answer is the following: in quantum silicon photonics, spiral waveguide results have better performances in indistinguishability than microring resonators. This result is quantified by the computed JSA overlaps of 98% with waveguides and 89% with microring resonators; see Table 1.

The purity of the generated photon pairs plays a significant role when the generated photons have to interfere with photons produced by other independent photon sources [20,21]. However, in a generic quantum application it is desirable to

have large values for both the purity and the indistinguishability because of the requirement of high visibility for dependent as well as independent sources. In our devices, we have seen two opposite cases: on one hand, a high visibility and JSA overlap but a low purity and low brightness (waveguide-based photon-pair sources), while on the other hand a low visibility and JSA overlap but a high purity (microring based photon-pair sources). This prevents qualifying one source as better than the other *a priori*. However, in the NISQ era of quantum computing one can simply choose what is needed to solve a task. Indeed, NISQ involves small numbers of qubits and algorithms that are focused on solving specific problems. One example is the variational quantum eigensolver [49,50], where what matters is the degree of indistinguishability and not the purity parameter. More generally, in applications where we create a photon pair in a superposition between different sources' paths, similarly to what happens in our SiPICs, the quantum interference is influenced by how much more indistinguishable the sources are. On the other hand, in applications like Boson sampling [51,52], where a large number of single (heralded) photons are required and the probability to inject a single photon state is proportional to the purity, one needs high values of purity. This brings us to the idea of application-tailored sources, i.e., sources designed for a specific algorithm and chosen to balance the required properties and the implementation efforts. Following this idea, the ideal would be to have a library of photon-pair sources classified according to their main characteristics and to choose the photon-pair source depending on the target class of problems and on the available fabrication resources.

From this point of view, our method can be understood as a quantifier for the indistinguishability of two sources, and it can be generalized for the indistinguishability test of more than two sources since the pair-wise test does not guarantee the overall indistinguishability of the sources [53,54]. The generalization can be achieved by parallelizing more sources and bringing the superposition of pairs into a suitable network of MZIs. Related to that, other applications of the experimental scheme and the theoretical model can be found in the many-particle quantum interference investigations [55–57].

APPENDIX A

A.1. Joint Spectral Amplitude and Single-Mode Squeezed State

The joint spectral amplitude (JSA) describes how photon-pairs are correlated [38,58]. It quantifies the probability density for the generation of one of the two photons in the ω_1-frequency state given the second photon in the ω_2-frequency state. The generic bi-photon state takes the following form:

$$|\Psi\rangle = \int \mathrm{d}\omega_1 \mathrm{d}\omega_2 F(\omega_1,\omega_2)\hat{a}^\dagger(\omega_1)\hat{a}^\dagger(\omega_2)|\mathrm{vac}\rangle, \tag{A1}$$

where

$$\langle\Psi|\Psi\rangle = \int \mathrm{d}\omega_1 \mathrm{d}\omega_2 |F(\omega_1,\omega_2)|^2 = 1.$$

F is the JSA, and $\hat{a}^\dagger(\omega)$ is the creation operator. The joint spectral intensity (JSI) is the modulus square of the JSA, i.e., $|F(\omega_s,\omega_i)|^2$. The JSI is directly linked to the intensity of the field, which is a measurable quantity.

Using the Schmidt decomposition for the JSA and two complete sets of orthonormal functions $\{u_n^{(1/2)}\}$ (the bar on a symbol stands for the complex conjugate of that quantity),

$$F(\omega_1,\omega_2) = \sum_\lambda \sqrt{r_\lambda}\, u_\lambda^{(1)}(\omega_1)u_\lambda^{(2)}(\omega_2), \tag{A2}$$

where

$$\int \mathrm{d}\omega u_{\lambda_1}^{(1/2)}(\omega)\bar{u}_{\lambda_2}^{(1/2)}(\omega) = \delta_{\lambda_1\lambda_2} \qquad \text{and} \qquad \sum_\lambda r_\lambda = 1,$$

and the bi-photon state can be written as a sum of product states,

$$|\Psi\rangle = \sum_\lambda \sqrt{r_\lambda}\left[\int \mathrm{d}\omega_1 u_\lambda^{(1)}(\omega_1)\hat{a}^\dagger(\omega_1)\right] \times \left[\int \mathrm{d}\omega_2 u_\lambda^{(2)}(\omega_2)\hat{a}^\dagger(\omega_2)\right]|\mathrm{vac}\rangle. \tag{A3}$$

The set of coefficients $\{r_\lambda\}$ are called the Schmidt coefficients. Finally, the purity of the bi-photon state is given by

$$P = \int \mathrm{d}\omega_1 \mathrm{d}\omega_2 \mathrm{d}\omega_1' \mathrm{d}\omega_2' F(\omega_1,\omega_2) \times \bar{F}(\omega_1,\omega_2')F(\omega_1',\omega_2')\bar{F}(\omega_1',\omega_2) = \sum_\lambda r_\lambda^2. \tag{A4}$$

This parameter is less than or equal to 1 and quantifies how much the state is factorizable. Note that taking the partial trace of the density matrix corresponding to the state in Eq. (A3), we obtain

$$\begin{aligned}\hat{\rho}_2 &:= \mathrm{Tr}_1|\Psi\rangle\langle\Psi| \\ &= \int \mathrm{d}\omega_2 \mathrm{d}\omega_2' \left[\int \mathrm{d}\omega_1 F(\omega_1,\omega_2)\bar{F}(\omega_1,\omega_2')\right] \\ &\quad \times \hat{a}^\dagger(\omega_2)|\mathrm{vac}\rangle\langle\mathrm{vac}|\hat{a}(\omega_2') \\ &= \sum_\lambda r_\lambda \left[\int \mathrm{d}\omega_2 u_\lambda^{(2)}(\omega_2)\hat{a}^\dagger(\omega_2)\right]|\mathrm{vac}\rangle \\ &\quad \times \langle\mathrm{vac}|\left[\int \mathrm{d}\omega_2' \bar{u}_\lambda^{(2)}(\omega_2')\hat{a}(\omega_2')\right].\end{aligned} \tag{A5}$$

From the previous equations, it is evident that we have a pure state after the application of a partial trace on the bi-photon state when only one Schmidt coefficient is equal to one and all the others are null. Therefore, when we are dealing with a source of bi-photon states, the purity parameter gives quantitative information about how much the state of a single photon in the pair is pure. It is an intrinsic property of the state and can be extended to the source. In particular, in the process of heralding, it is used to express the quality of the source of photons in the production of single-photon states.

Another important characteristic of photon sources is their indistinguishability, which is an extrinsic property since it is evaluated through the comparison of different sources. A good estimator for it is given by the overlap between the JSAs of the bi-photon states produced by different sources. This idea can be naively associated with the comparison of two normalized vectors through their scalar product.

It is natural to use the previous concepts in nonlinear spontaneous parametric processes, where the bi-photon state is generated by converting pump photons into the correlated signal and idler pair of photons. In particular, the SFWM process is described by the following Hamiltonian [27,38]:

$$\begin{aligned} H_{\mathrm{FWM}} = & -\frac{\gamma_{SIP_1P_2}\hbar^2\omega_{SIP_1P_2}}{4\pi^2} \\ & \times \int \mathrm{d}x\mathrm{d}\omega_1\mathrm{d}\omega_2\mathrm{d}\omega_3\mathrm{d}\omega_4 e^{i(\omega_1+\omega_2-\omega_3-\omega_4)t} \\ & \times e^{-i[k_S(\omega_1)+k_I(\omega_2)-k_{P_1}(\omega_3)-k_{P_2}(\omega_4)]x} \\ & \times a_s^\dagger(\omega_1)a_i^\dagger(\omega_2)a_{P_1}(\omega_3)a_{P_2}(\omega_4) + \mathrm{h.c.}, \end{aligned} \tag{A6}$$

where

$$\omega_{SIP_1P_2} = (\omega_s\omega_i\omega_{P_1}\omega_{P_2})^{1/4}, \qquad \gamma_{SIP_1P_2} = n_2\frac{\omega_{SIP_1P_2}}{c\mathcal{A}^{\mathrm{eff}}_{SIP_1P_2}}. \tag{A7}$$

$\mathcal{A}^{\mathrm{eff}}$ is the effective area of the process, k is the wavevector of the four photons, n_2 is the nonlinear refractive index of the material, and γ is the parameter that characterizes the strength of the FWM process [27].

In SFWM, we can have two different cases: the non-degenerate case where the pump photons are degenerate in frequency and the generated pair is not, and the degenerate case where we have the opposite situation. In the experiment, we are interested in the case where two pump photons ($P_{1/2}$) are converted into two photons (s and i) with the same frequency. This means that our JSA is a symmetric function and $u := u^{(1)} = u^{(2)}$.

In the low-gain regime and for coherent laser pumps (thus the pump is treated classically), the final state is a squeezed state,

$$|\Psi\rangle = \hat{\mathcal{U}}|\mathrm{vac}\rangle, \quad \text{where}$$

$$\hat{\mathcal{U}} = \exp\left[\frac{1}{2}\xi\int \mathrm{d}\omega_s\mathrm{d}\omega_i F(\omega_s,\omega_i)\hat{a}^\dagger(\omega_s)\hat{a}^\dagger(\omega_i) - \mathrm{h.c.}\right], \tag{A8}$$

where ξ is the squeezing parameter, and $F(\omega_s,\omega_i)$ is the bi-photon wavefunction or JSA. In our case, the JSA can be written as

$$F(\omega_s,\omega_i) = \int \mathrm{d}\omega\alpha(\omega)\beta(\omega_s+\omega_i-\omega)\phi(\omega_s,\omega_i,\omega), \tag{A9}$$

where $\alpha(\omega)$ and $\beta(\omega)$ are the complex amplitudes of the pump beams, and the function ϕ is the phase matching function given by the following relation:

$$\phi(\omega_s,\omega_i,\omega) = \exp\left[\frac{i\Delta k(\omega_s,\omega_i,\omega)L}{2}\right]\mathrm{sinc}\left[\frac{\Delta k(\omega_s,\omega_i,\omega)L}{2}\right], \tag{A10}$$

L is the waveguide length and Δk is the phase mismatch parameter [59]. As we can see from (A9), the JSA receives two contributions: one from the shape of the pump beams and one from the phase matching function that contains the kinematic parameter Δk. In the microring resonator case [42,60], Eq. (A9) takes a slightly different form to account for the enhancement effect due to the microring, in particular

$$\begin{aligned} & F(\omega_s,\omega_i) \\ & = l_s(\omega_s)l_i(\omega_i)\int \mathrm{d}\omega\alpha(\omega)l_{p_1}(\omega)\beta(\omega_s+\omega_i-\omega)l_{p_2}(\omega_s+\omega_i-\omega), \end{aligned} \tag{A11}$$

where $l_j(\omega)$ is the Lorentzian function relative to the microring resonance linewidth of the jth resonance involved in the process. Again, the JSA quantifies the probability density for the creation of the pair's first photon in the ω_s mode and the second photon in the ω_i mode. Using Eq. (A2), we can write the state as

$$\begin{aligned} |\Psi\rangle &= \exp\left(\frac{1}{2}\sum_\lambda \xi_\lambda \hat{A}_\lambda^2 - \mathrm{h.c.}\right)|\mathrm{vac}\rangle \\ &= \bigotimes_\lambda\left[\frac{1}{\sqrt{\cosh\ \xi_\lambda}}\sum_{n=0}^{\infty}(\tanh\ \xi_\lambda)^n\frac{\sqrt{(2n)!}}{2^n n!}|2n\rangle_\lambda\right], \end{aligned} \tag{A12}$$

where

$$\xi_\lambda := \xi\sqrt{r_\lambda}, \qquad |n\rangle_\lambda := \frac{1}{\sqrt{n!}}(\hat{A}_\lambda)^n|\mathrm{vac}\rangle \qquad \text{and}$$

$$\hat{A}_\lambda := \int \mathrm{d}\omega u_\lambda(\omega)\hat{a}^\dagger(\omega). \tag{A13}$$

The squeezing parameter contains the information about the pair-generation probability. Note that by expanding Eq. (A8) for small squeezing and keeping only the first non-trivial term, we have the same form of Eq. (A1).

From the following statistic distribution, it is possible to obtain the main properties:

$$\langle\hat{n}\rangle = \sum_\lambda(\sinh\ \xi_\lambda)^2, \tag{A14}$$

$$p_{\mathrm{trig}} = 1 - \sum_\lambda \mathrm{sech}\xi_\lambda, \tag{A15}$$

where p_{trig} is the probability to activate a threshold detector. Finally, we are now ready to take into account the effect of the losses. Each lossy component is modeled as an ideal component preceded by an ideal beamsplitter with a non-unit transmission probability,

$$\hat{A}_\lambda \to \eta_\lambda\hat{A}_\lambda + \sqrt{1-\eta_\lambda^2}\hat{e}_\lambda, \tag{A16}$$

where $0 \le \eta_\lambda \le 1$ is the transmission, and $\hat{e}_\lambda$ is the destruction operator of the environment. The full state, after accounting for losses and tracing over environment modes, can therefore be written as

$$\begin{aligned} \hat{\rho} &= \otimes_\lambda \hat{\rho}_\lambda, \\ \hat{\rho}_\lambda &= \frac{1}{\cosh\ \xi_\lambda}\sum_{n=0}^{\infty}(\tanh\ \xi_\lambda)^{2n}\left[\frac{(2n)!}{2^n n!}\right]^2 \\ & \quad \times \sum_{k=0}^{n}\frac{\eta_\lambda^{2(2n-k)}(1-\eta_\lambda^2)^k}{k!(2n-k)!}|2n-k\rangle_\lambda\langle 2n-k|_\lambda. \end{aligned} \tag{A17}$$

The previous properties are then modified in the following way:

$$\langle\hat{n}\rangle = \sum_\lambda \eta_\lambda^2(\sinh\ \xi_\lambda)^2, \tag{A18}$$

$$p_{\text{trig}} = 1 - \sum_{\lambda} \frac{\operatorname{sech}\ \xi_\lambda}{\sqrt{1-(1-\eta_\lambda)^2(\tanh\ \xi_\lambda)^2}}. \tag{A19}$$

A.2. Evolution State Description in the Reverse HOM Interference Experiment

In this section, we examine the theoretical underpinnings of the reverse HOM interference phenomenon [23–25] as seen in the integrated system shown in Fig. 1(a). Therefore, for simplicity, we restrict ourselves to the waveguide source case only. The extension to the microring source is straightforward. In this subsection, photon creation through the SFWM process is described using the notation contained in the previous subsection. In order to follow the evolution of the state step-by-step, we divide the integrated silicon chip into five distinct sections, denoted by the Roman numerals I through V, as shown in Fig. 10. In Section I, the pump photons are divided into two paths, path 1 (upper) and path 2 (lower), by the first 1 × 2 MMI. In Section II, the degenerate SFWM process produces the pair of photons along the two paths. Through the use of a phase shifter, path 1 in Section III gains a relative phase with respect to path 2. A 2 × 2 MMI in Section IV causes interference between the photons propagating in the two arms. Finally, the filtering and detection of the two pathways are carried out in Section V.

The initial state composed of two pump beams at the two frequencies, ω_{P1} and ω_{P2}, can be described as

$$|\Psi\rangle_0 = \exp\left\{\int \mathrm{d}\omega[\alpha(\omega)+\beta(\omega)]\hat{A}^\dagger(\omega)\right\}|\text{vac}\rangle, \tag{A20}$$

where $\hat{A}^\dagger(\omega)$ is the creation operator, and α and β are the pump's amplitude functions centered at ω_{P1} and ω_{P2}. Note that we are working with unnormalized states, and therefore any meaningful quantity must result from a proper ratio.

Because of the filter at the entrance of the chip, we can assume that

$$\int \mathrm{d}\omega\alpha(\omega)\tilde{\beta}(\omega) = 0. \tag{A21}$$

In Section I the pump photons interfere with a 1 × 2 MMI. By applying this evolution to the initial state, we obtain

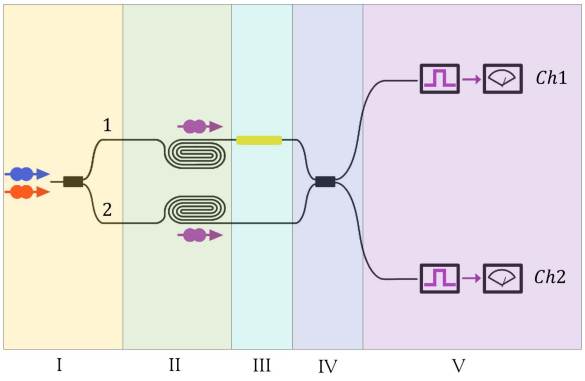

Fig. 10. Scheme presented in Fig. 1(a). Its division into 5 parts is beneficial for its analytical description.

$$|\Psi\rangle_{\text{I}} = \exp\left\{\int \mathrm{d}\omega\frac{\alpha(\omega)+\beta(\omega)}{\sqrt{2}}[\hat{a}_1^\dagger(\omega)+\hat{a}_2^\dagger(\omega)]\right\}|\text{vac}\rangle, \tag{A22}$$

where $\hat{a}_1^\dagger$ corresponds to the upper waveguide and $\hat{a}_2^\dagger$ to the lower one.

In Section II the FWM mechanism generates correlated photons that annihilate two pump photons. As we explained in the previous subsection, the state is

$$|\Psi\rangle_{\text{II}} = \exp\left\{\frac{\xi}{2}\int \mathrm{d}\omega_i\mathrm{d}\omega_s[F_1(\omega_i,\omega_s)\hat{a}_1^\dagger(\omega_i)\hat{a}_1^\dagger(\omega_s) + F_2(\omega_i,\omega_s)\hat{a}_2^\dagger(\omega_i)\hat{a}_2^\dagger(\omega_s)]\right\}|\text{vac}\rangle, \tag{A23}$$

where $F_{1/2}$ is the JSA of the source in the upper/lower waveguides. We neglect the residual contribution from the pumps and the non-degenerate generation process since our detection will capture only the contributions around the degenerate generation process.

In Section III, a phase shifter is introduced into path 1. This enables the photons from that path to undergo an additional phase shift. The resultant state will be

$$|\Psi\rangle_{\text{III}} = \exp\left\{\frac{\xi}{2}\int \mathrm{d}\omega_i\mathrm{d}\omega_s[F_1(\omega_i,\omega_s)e^{2i\phi}\hat{a}_1^\dagger(\omega_i)\hat{a}_1^\dagger(\omega_s) + F_2(\omega_i,\omega_s)\hat{a}_2^\dagger(\omega_i)\hat{a}_2^\dagger(\omega_s)]\right\}|\text{vac}\rangle. \tag{A24}$$

At this point, in Section IV, the interference of the two routes 1 and 2 through a 2 × 2 MMI is discussed, whose behavior on its two inputs may be analytically defined as follows:

$$\hat{a}_1^\dagger \to \frac{1}{\sqrt{2}}(\hat{a}_1^\dagger + i\hat{a}_2^\dagger), \qquad \hat{a}_2^\dagger \to \frac{1}{\sqrt{2}}(\hat{a}_2^\dagger + i\hat{a}_1^\dagger). \tag{A25}$$

Applying these transformations, the state will evolve as follows:

$$\begin{aligned}
&|\Psi\rangle_{\text{IV}} \\
&= \exp\left\{\frac{\xi}{4}\int \mathrm{d}\omega_i\mathrm{d}\omega_s\{F_1(\omega_i,\omega_s)e^{2i\phi}[\hat{a}_1^\dagger(\omega_i) + i\hat{a}_2^\dagger(\omega_i)][\hat{a}_1^\dagger(\omega_s) + i\hat{a}_2^\dagger(\omega_s)] + F_2(\omega_i,\omega_s)[\hat{a}_2^\dagger(\omega_i) + i\hat{a}_1^\dagger(\omega_i)][\hat{a}_2^\dagger(\omega_s) + i\hat{a}_1^\dagger(\omega_s)]\}\right\}|\text{vac}\rangle \\
&= \exp\left\{\frac{\xi}{4}\int \mathrm{d}\omega_i\mathrm{d}\omega_s\{[F_1(\omega_i,\omega_s)e^{2i\phi} - F_2(\omega_i,\omega_s)][\hat{a}_1^\dagger(\omega_i)\hat{a}_1^\dagger(\omega_s) - \hat{a}_2^\dagger(\omega_i)\hat{a}_2^\dagger(\omega_s)] + 2i[F_1(\omega_i,\omega_s)e^{2i\phi} + F_2(\omega_i,\omega_s)]\hat{a}_1^\dagger(\omega_i)\hat{a}_2^\dagger(\omega_s)\}\right\}|\text{vac}\rangle.
\end{aligned} \tag{A26}$$

The filtering and detection is represented by the operators

$$\hat{P}_i := \int \mathrm{d}\omega f(\omega)\sum_{n\neq 0}\frac{1}{n!}[\hat{a}_i(\omega)^\dagger]^n|\text{vac}\rangle\langle\text{vac}|[\hat{a}_i(\omega)]^n, \tag{A27}$$

where the function f represents the spectral amplitude of the filter. Note that we have implemented operators that take into account threshold detectors.

The probability of detecting coincidences in channels 1 and 2 [Fig. 1(a)] is given by

$$p_{12} = \frac{\mathrm{Tr}\{|\psi^{\mathrm{out}}\rangle\langle\psi^{\mathrm{out}}|\hat{P}_1 \otimes \hat{P}_2\}}{\mathrm{Tr}\{|\psi^{\mathrm{out}}\rangle\langle\psi^{\mathrm{out}}|\}} = \frac{\langle\psi^{\mathrm{out}}|\hat{P}_1 \otimes \hat{P}_2|\psi^{\mathrm{out}}\rangle}{\langle\psi^{\mathrm{out}}|\psi^{\mathrm{out}}\rangle}$$
$$\approx \frac{1}{4}\int \mathrm{d}\omega_i \mathrm{d}\omega_s f(\omega_i) f(\omega_s)\{|F_1(\omega_i,\omega_s)|^2 + |F_2(\omega_i,\omega_s)|^2 + 2\,\mathrm{Re}[F_1(\omega_i,\omega_s)\bar{F}_2(\omega_i,\omega_s)e^{2i\phi}]\}$$
$$= \frac{1}{2}\left\{1 + \mathrm{Re}\left[e^{2i\phi}\int \mathrm{d}\omega_i \mathrm{d}\omega_s f(\omega_i) f(\omega_s) \times F_1(\omega_i,\omega_s)\bar{F}_2(\omega_i,\omega_s)\right]\right\}. \quad \textbf{(A28)}$$

The approximation consisting of keeping only the leading term is based on the fact that we can choose to work in the low-gain regime once the sources have been characterized.

We conclude this subsection by writing the visibility in terms of the JSA overlaps. First, the visibility V is defined as [24]

$$V = \frac{p_{12}^{\max} - p_{12}^{\min}}{p_{12}^{\max}}. \quad \textbf{(A29)}$$

This definition has been chosen in the analysis of the experimental data, but there are other choices [61] that lead to different values of visibility. Nevertheless, in our cases the visibility can be linked to a physical quantity that is independent from any convention.

In terms of the JSA overlaps, p_{12} takes the form

$$p_{12}(\phi,\delta,N) = \frac{1}{2}[1 + N\cos(2\phi+\delta)], \quad \textbf{(A30)}$$

where

$$Ne^{i\delta} := \int \mathrm{d}\omega_i \mathrm{d}\omega_s f(\omega_i) f(\omega_s) F_1(\omega_i,\omega_s)\bar{F}_2(\omega_i,\omega_s). \quad \textbf{(A31)}$$

It is easy to see that $F_1 = F_2$ implies $N = 1$ and $\delta = 0$ and, therefore, $p_{12} = \cos^2\phi$, $p_{12}^{\max} = p_{12}(\phi = 0)$, and $p_{12}^{\min} = p_{12}(\phi = \pi/2)$.

In the generic case, the maxima of p_{12} are located at $2\phi + \delta = 2N\pi$ and the minima at $2\phi + \delta = N\pi$ with $N \in \mathbf{Z}$, and the visibility reads as

$$V = \frac{2N}{1+N}, \quad \textbf{(A32)}$$

where

$$N := \left|\int \mathrm{d}\omega_i \mathrm{d}\omega_s f(\omega_i) f(\omega_s) F_1(\omega_i,\omega_s)\bar{F}_2(\omega_i,\omega_s)\right|. \quad \textbf{(A33)}$$

Therefore, knowing the experimental value for V, it is possible to deduce N as we did in Table 1 of the main text where the computed JSA overlaps for our sources are reported.

The normalized coincidence probability reads

$$p_{12}^{\mathrm{norm}}(\phi,\delta,N) = \frac{1}{1+N}[1 + N\cos(2\phi+\delta)]. \quad \textbf{(A34)}$$

This formula has been used to build the theoretical results in Figs. 6(b), 7(b), 7(c), and 8.

From the formula for the normalized coincidence probability, we can note that a relative phase difference between the JSA of the two sources can shift the interference pattern of the HOM experiment. Of course, such relative phase can be easily hidden from our observation because of non-idealities due to the fabrication. In our case, a small difference in the length of the two arms of the MZI involved in the HOM dynamics should provide a large contribution.

A.3. Evolution State Description in the Reverse HOM-HOM-Reverse HOM Experiment

In this section, we examine the theoretical underpinnings [23–25] of the reverse HOM-HOM-reverse HOM experiment as seen in the integrated system shown in Figs. 1(c) and 2(a).

As we have done in the previous subsection, we divided the integrated system in different sections. Note that by changing ϕ to ϕ_1, the design is the same until Section IV. In Section V, the two paths are divided into other two paths through two 1×2 MMIs. At this step, path 1 is split into two new paths, which will be denoted as path 1 (corresponding to detection channel 1) and path 3 (corresponding to detection channel 3), and analogously path 2 into path 4 (corresponding to detection channel 4) and path 2 (corresponding to detection channel 2). In Section VI, an integrated MZI made up of two 2×2 MMIs and a phase shifter causes photons from paths 3 and 4 to interact. The filtering and detection of the four pathways are carried out in the final Section VII.

Let us start from the state in Section IV, where

$$|\Psi\rangle_{\mathrm{IV}} = \exp\left\{\frac{\xi}{4}\int \mathrm{d}\omega_i \mathrm{d}\omega_s \{F_1(\omega_i,\omega_s)e^{2i\phi}[\hat{a}_1^\dagger(\omega_i) + i\hat{a}_2^\dagger(\omega_i)][\hat{a}_1^\dagger(\omega_s) + i\hat{a}_2^\dagger(\omega_s)] + F_2(\omega_i,\omega_s)[\hat{a}_2^\dagger(\omega_i) + i\hat{a}_1^\dagger(\omega_i)][\hat{a}_2^\dagger(\omega_s) + i\hat{a}_1^\dagger(\omega_s)]\}\right\}|\mathrm{vac}\rangle. \quad \textbf{(A35)}$$

In Section V, we have two 1×2 MMI described as

$$\hat{a}_1^\dagger \to \frac{1}{\sqrt{2}}(\hat{a}_1^\dagger + \hat{a}_3^\dagger), \quad \hat{a}_2^\dagger \to \frac{1}{\sqrt{2}}(\hat{a}_4^\dagger + \hat{a}_2^\dagger), \quad \textbf{(A36)}$$

where with an abuse of notation $\hat{a}_1^\dagger$ corresponds to the external upper waveguide, $\hat{a}_3^\dagger$ to the central upper one, $\hat{a}_4^\dagger$ to the central lower one, and $\hat{a}_2^\dagger$ to the external lower one (see the corresponding detection channels in Fig. 11). Thus, at Section V the state will be

$$|\Psi\rangle_{\mathrm{V}} = \exp\left\{\frac{\xi}{8}\int \mathrm{d}\omega_i \mathrm{d}\omega_s [F_1(\omega_i,\omega_s)e^{2i\phi_1}\hat{b}_1^\dagger(\omega_i)\hat{b}_1^\dagger(\omega_s) - F_2(\omega_i,\omega_s)\hat{b}_2^\dagger(\omega_i)\hat{b}_2^\dagger(\omega_s)]\right\}|\mathrm{vac}\rangle,$$

where

$$\hat{b}_1^\dagger(\omega) \equiv \hat{a}_1^\dagger(\omega) + \hat{a}_3^\dagger(\omega) + i\hat{a}_4^\dagger(\omega) + i\hat{a}_2^\dagger(\omega),$$
and $$\hat{b}_2^\dagger(\omega) \equiv \hat{a}_1^\dagger(\omega) + \hat{a}_3^\dagger(\omega) - i\hat{a}_4^\dagger(\omega) - i\hat{a}_2^\dagger(\omega).$$

The second MZI in Section VI solely acts on photons traveling along pathways $\hat{a}_3$ and $\hat{a}_4$. Therefore, the resulting state in Section VI reads as

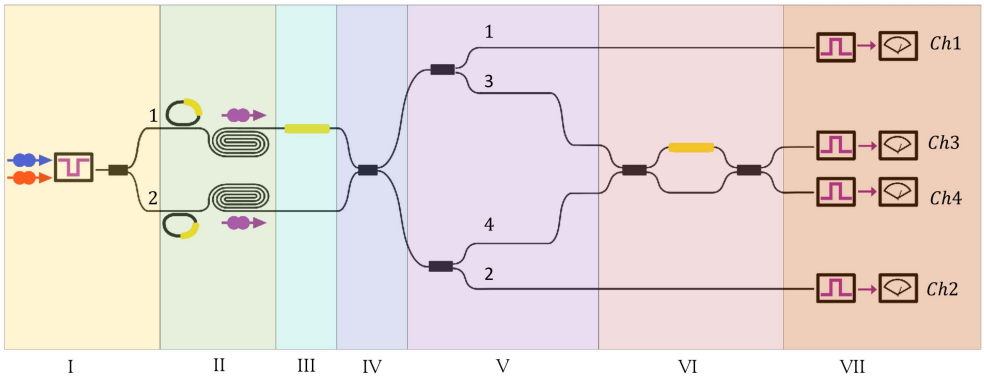

Fig. 11. Chip design shown in Fig. 1(c) is displayed. It is divided into 7 parts for simplicity of discussion.

$$|\Psi\rangle_{\mathrm{VI}} = \exp\left\{\frac{\xi}{8}\int \mathrm{d}\omega_i \mathrm{d}\omega_s [F_1(\omega_i,\omega_s)e^{2i\phi_1}\hat{b}_3^\dagger(\omega_i)\hat{b}_3^\dagger(\omega_s) - F_2(\omega_i,\omega_s)\hat{b}_4^\dagger(\omega_i)\hat{b}_4^\dagger(\omega_s)]\right\}|\mathrm{vac}\rangle,$$

where

$$\hat{b}_3^\dagger(\omega) \equiv \hat{a}_1^\dagger(\omega) - \hat{a}_3^\dagger(\omega) + i\hat{a}_4^\dagger(\omega) + i\hat{a}_2^\dagger(\omega),$$

and

$$\hat{b}_4^\dagger(\omega) \equiv \hat{a}_1^\dagger(\omega) + e^{i\phi_2}(\hat{a}_3^\dagger(\omega) + i\hat{a}_4^\dagger(\omega)) - i\hat{a}_2^\dagger(\omega).$$

The final state for the scheme shown in Fig. 2(a) can be found tracing out the photons in channels 1 and 2, since, in that case, the 1×2 MMIs are substituted by asymmetric MZIs for pump removals that do not affect the generated photons. Between the schemes in Figs. 1(c) and 2(a), the formula for the visibility does not change as long as we replace ch 3 and ch 4 of Fig. 1(c) with ch 1 and ch 2 of Fig. 2(a), respectively.

The filtering and detection is represented by the operators defined in Eq. (A27), where the function f represents the spectral amplitude of the filter.

The probability of detecting channels i and j is given by

$$p_{ij} = \frac{\mathrm{Tr}\{|\psi^{\mathrm{out}}\rangle\langle\psi^{\mathrm{out}}|\hat{P}_i\otimes\hat{P}_j\}}{\mathrm{Tr}\{|\psi^{\mathrm{out}}\rangle\langle\psi^{\mathrm{out}}|\}} = \frac{\langle\psi^{\mathrm{out}}|\hat{P}_i\otimes\hat{P}_j|\psi^{\mathrm{out}}\rangle}{\langle\psi^{\mathrm{out}}|\psi^{\mathrm{out}}\rangle}. \tag{A37}$$

If we consider the probability after Section VII, then

$$p_{13} = p_{24} = \frac{1}{8}\int \mathrm{d}\omega_i \mathrm{d}\omega_s f(\omega_i)f(\omega_s) \times \{|F_1(\omega_i,\omega_s)|^2 + |F_2(\omega_i,\omega_s)|^2 + 2\,\mathrm{Re}[F_1(\omega_i,\omega_s)\bar{F}_2(\omega_i,\omega_s)e^{i(2\phi_1-\phi_2)}]\},$$

$$p_{14} = p_{23} = \frac{1}{8}\int \mathrm{d}\omega_i \mathrm{d}\omega_s f(\omega_i)f(\omega_s) \times \{|F_1(\omega_i,\omega_s)|^2 + |F_2(\omega_i,\omega_s)|^2 - 2\,\mathrm{Re}[F_1(\omega_i,\omega_s)\bar{F}_2(\omega_i,\omega_s)e^{i(2\phi_1-\phi_2)}]\},$$

$$p_{12} = \frac{1}{8}\int \mathrm{d}\omega_i \mathrm{d}\omega_s f(\omega_i)f(\omega_s) \times \{|F_1(\omega_i,\omega_s)|^2 + |F_2(\omega_i,\omega_s)|^2 + 2\,\mathrm{Re}[F_1(\omega_i,\omega_s)\bar{F}_2(\omega_i,\omega_s)e^{2i\phi_1}]\},$$

$$p_{34} = \frac{1}{8}\int \mathrm{d}\omega_i \mathrm{d}\omega_s f(\omega_i)f(\omega_s) \times \{|F_1(\omega_i,\omega_s)|^2 + |F_2(\omega_i,\omega_s)|^2 + 2\,\mathrm{Re}[F_1(\omega_i,\omega_s)\bar{F}_2(\omega_i,\omega_s)e^{2i(\phi_1-\phi_2)}]\},$$

where the 4 detectors are represented by the indices 1, 2, 3, and 4. Detectors 1 and 2 are specifically the outside detectors that correspond to pathways a_1 and a_2. Detectors 3 and 4 make up the two central detectors corresponding to the two paths a_3 and a_4. We can rewrite p_{34} and p_{12} as

$$p_{12} = \frac{1}{8}\left\{1 + \mathrm{Re}\left[e^{2i\phi_1}\int \mathrm{d}\omega_i \mathrm{d}\omega_s f(\omega_i)f(\omega_s) \times F_1(\omega_i,\omega_s)\bar{F}_2(\omega_i,\omega_s)\right]\right\}, \tag{A38}$$

$$p_{34} = \frac{1}{8}\left\{1 + \mathrm{Re}\left[e^{2i(\phi_1-\phi_2)}\int \mathrm{d}\omega_i \mathrm{d}\omega_s f(\omega_i)f(\omega_s) \times F_1(\omega_i,\omega_s)\bar{F}_2(\omega_i,\omega_s)\right]\right\}. \tag{A39}$$

The visibility is defined as

$$V = \frac{p_{34}^{\max} - p_{34}^{\min}}{p_{34}^{\max}}, \tag{A40}$$

and doing the same manipulation as in Section A.2, we can arrive at the same formulas. The same conclusion is due to the fact that all the designs exploit the same features once the data of the coincidences are normalized.

A.4. Impact of Pump Noise and Fabrication Imperfections on the Visibility and JSA Overlaps

In this section, we want to investigate how the presence of unwanted pump noise can affect the visibility of the interference pattern of the coincidence measurements. We model such noise as an additional contribution to the density matrix given by the desired output state $|\psi_{\mathrm{out}}\rangle$ obtained at the end of the manipulation done on the PIC. The total density matrix reads

$$\rho_{\mathrm{tot}} = c|\psi_{\mathrm{out}}\rangle\langle\psi_{\mathrm{out}}| + (1-c)\rho_{\mathrm{noise}}, \tag{A41}$$

where c is a visibility parameter that depends on the signal-to-noise ratio, CAR, and the experimental setup, and ρ_{noise} represents the noise contribution at the output. The probability of

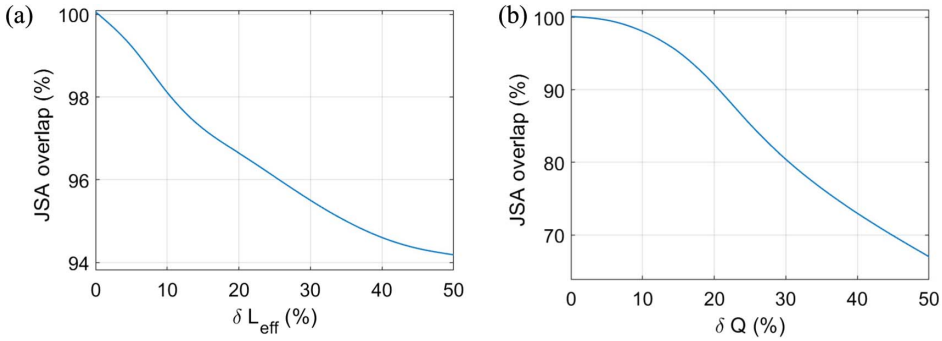

Fig. 12. (a) Simulated JSA overlaps as a function of the variations of L_{eff} for spiral waveguides. (b) JSA overlaps as a function of the variations of the Q-factor for microring resonators.

detecting in channels i and j is modified and has the following form:

$$p_{ij} = \frac{\text{Tr}\{\rho_{\text{tot}}\hat{P}_i \otimes \hat{P}_j\}}{\text{Tr}\{\rho_{\text{tot}}\}} = \frac{c\langle\psi^{\text{out}}|\hat{P}_i \otimes \hat{P}_j|\psi^{\text{out}}\rangle + (1-c)\text{Tr}\{\rho_{\text{noise}}\hat{P}_i \otimes \hat{P}_j\}}{\text{Tr}\{\rho_{\text{tot}}\}}. \tag{A42}$$

Using the definition of visibility we proposed in this work and the results of the previous subsections, we obtain

$$V = \frac{2N}{1+N+D}, \tag{A43}$$

where N is the JSA overlap given in Eq. (A33), and D is a parameter constructed from $\text{Tr}\{\rho_{\text{noise}}\hat{P}_i \otimes \hat{P}_j\}$ and c. The previous equation is obtained assuming that the noisy part depends weakly on the ϕ phases, and it shows qualitatively lower visibility for higher noise, i.e., $c \to 0$. In Fig. 8 of Section 5, we show how the visibility increases thanks to the improved filtering of the residual pump through an a-MZI and a consequent better CAR value. For future investigations, it would be interesting to link the parameter D to the CAR and quantitatively estimate its contribution. However, this goes beyond the scope of this paper and is left for further studies.

Finally, in Fig. 12, we report the plots showing the behavior of the JSA overlaps assuming deviations in the parameters of one of the two sources. In particular, for spiral waveguides we consider variations of L_{eff} ($\delta L_{\text{eff}} = \Delta L_{\text{eff}}^{\text{error}}/L_{\text{eff}}^{\text{nominal}}$ [%]), while for microring resonators we consider variations of the Q-factor ($\delta Q = \Delta Q^{\text{error}}/Q^{\text{nominal}}$ [%]).

Funding. Horizon 2020 Framework Programme (899368); National Research Foundation of Korea (2022M3E4A1083526, 2020M3E4A107845); Electronics and Telecommunications Research Institute (23YB1300).

Disclosures. The authors declare no conflicts of interest.

Data Availability. Data underlying the results presented in this paper are not publicly available at this time but may be obtained from the authors upon reasonable request.

REFERENCES

1. B. Shaw, M. M. Wilde, O. Oreshkov, I. Kremsky, and D. A. Lidar, "Encoding one logical qubit into six physical qubits," Phys. Rev. A **78**, 012337 (2008).
2. L. Viola, E. Knill, and R. Laflamme, "Constructing qubits in physical systems," J. Phys. A **34**, 7067–7079 (2001).
3. R. W. Heeres, P. Reinhold, N. Ofek, L. Frunzio, L. Jiang, M. H. Devoret, and R. J. Schoelkopf, "Implementing a universal gate set on a logical qubit encoded in an oscillator," Nat. Commun. **8**, 94 (2017).
4. D. Ristè, S. Poletto, M.-Z. Huang, A. Bruno, V. Vesterinen, O.-P. Saira, and L. DiCarlo, "Detecting bit-flip errors in a logical qubit using stabilizer measurements," Nat. Commun. **6**, 6983 (2015).
5. E. Kapit, "Hardware-efficient and fully autonomous quantum error correction in superconducting circuits," Phys. Rev. Lett. **116**, 150501 (2016).
6. B. Da Lio, C. Faurby, X. Zhou, M. L. Chan, R. Uppu, H. Thyrrestrup, S. Scholz, A. D. Wieck, A. Ludwig, P. Lodahl, and L. Midolo, "A pure and indistinguishable single-photon source at telecommunication wavelength," Adv. Quantum Technol. **5**, 2200006 (2022).
7. N. Lal, S. Mishra, and R. P. Singh, "Indistinguishable photons," AVS Quantum Sci. **4**, 021701 (2022).
8. S. Azzini, D. Grassani, M. J. Strain, M. Sorel, L. G. Helt, J. E. Sipe, M. Liscidini, M. Galli, and D. Bajoni, "Ultra-low power generation of twin photons in a compact silicon ring resonator," Opt. Express **20**, 23100–23107 (2012).
9. E. Engin, D. Bonneau, C. M. Natarajan, A. S. Clark, M. G. Tanner, R. H. Hadfield, S. N. Dorenbos, V. Zwiller, K. Ohira, N. Suzuki, H. Yoshida, N. Iizuka, M. Ezaki, J. L. O'Brien, and M. G. Thompson, "Photon pair generation in a silicon micro-ring resonator with reverse bias enhancement," Opt. Express **21**, 27826–27834 (2013).
10. S. Signorini and L. Pavesi, "On-chip heralded single photon sources," AVS Quantum Sci. **2**, 041701 (2020).
11. R. P. Feynman, "Simulating physics with computers," Int. J. Theor. Phys. **21**, 467–488 (1982).
12. T. H. Johnson, S. R. Clark, and D. Jaksch, "What is a quantum simulator?" EPJ Quantum Technol. **1**, 10 (2014).
13. R. Raussendorf and H. J. Briegel, "A one-way quantum computer," Phys. Rev. Lett. **86**, 5188–5191 (2001).
14. H. J. Briegel, D. Browne, W. Dür, and M. Van den Nest, "Measurement-based quantum computation," Nat. Phys. **5**, 19–26 (2009).
15. S. Bartolucci, P. Birchall, H. Bombin, H. Cable, C. Dawson, M. Gimeno-Segovia, E. Johnston, K. Kieling, N. Nickerson, M. Pant, F. Pastawski, T. Rudolph, and C. Sparrow, "Fusion-based quantum computation," arXiv, arXiv:2101.09310 (2021).
16. H. Bombin, I. H. Kim, D. Litinski, N. Nickerson, M. Pant, F. Pastawski, S. Roberts, and T. Rudolph, "Interleaving: Modular architectures for fault-tolerant photonic quantum computing," arXiv, arXiv:2103.08612 (2021).
17. C. Vigliar, S. Paesani, Y. Ding, J. C. Adcock, J. Wang, S. Morley-Short, D. Bacco, L. K. Oxenløwe, M. G. Thompson, J. G. Rarity,

and A. Laing, "Error-protected qubits in a silicon photonic chip," Nat. Phys. **17**, 1137–1143 (2021).
18. J. W. Silverstone, D. Bonneau, K. Ohira, N. Suzuki, H. Yoshida, N. Iizuka, M. Ezaki, C. M. Natarajan, M. G. Tanner, R. H. Hadfield, V. Zwiller, G. D. Marshall, J. G. Rarity, J. L. O'Brien, and M. G. Thompson, "On-chip quantum interference between silicon photon-pair sources," Nat. Photonics **8**, 104–108 (2014).
19. J.-M. Lee, W.-J. Lee, M.-S. Kim, and J. J. Ju, "Noise filtering for highly correlated photon pairs from silicon waveguides," J. Lightwave Technol. **37**, 5428–5434 (2019).
20. I. I. Faruque, G. F. Sinclair, D. Bonneau, J. G. Rarity, and M. G. Thompson, "On-chip quantum interference with heralded photons from two independent micro-ring resonator sources in silicon photonics," Opt. Express **26**, 20379–20395 (2018).
21. D. Llewellyn, Y. Ding, I. I. Faruque, S. Paesani, D. Bacco, R. Santagati, Y.-J. Qian, Y. Li, Y.-F. Xiao, M. Huber, M. Malik, G. F. Sinclair, X. Zhou, K. Rottwitt, J. L. O'Brien, J. G. Rarity, Q. Gong, L. K. Oxenlowe, J. Wang, and M. G. Thompson, "Chip-to-chip quantum teleportation and multi-photon entanglement in silicon," Nat. Phys. **16**, 148–153 (2020).
22. J.-M. Lee, W.-J. Lee, M.-S. Kim, S. Cho, J. J. Ju, G. Navickaite, and J. Fernandez, "Controlled-NOT operation of SiN-photonic circuit using photon pairs from silicon-photonic circuit," Opt. Commun. **509**, 127863 (2022).
23. C. K. Hong, Z. Y. Ou, and L. Mandel, "Measurement of subpicosecond time intervals between two photons by interference," Phys. Rev. Lett. **59**, 2044–2046 (1987).
24. A. M. Brańczyk, "Hong–Ou–Mandel interference," arXiv, arXiv:1711.00080 (2017).
25. F. Bouchard, A. Sit, Y. Zhang, R. Fickler, F. M. Miatto, Y. Yao, F. Sciarrino, and E. Karimi, "Two-photon interference: the Hong–Ou–Mandel effect," Rep. Prog. Phys. **84**, 012402 (2020).
26. J. He, B. A. Bell, A. Casas-Bedoya, Y. Zhang, A. S. Clark, C. Xiong, and B. J. Eggleton, "Ultracompact quantum splitter of degenerate photon pairs," Optica **2**, 779–782 (2015).
27. N. Quesada, L. G. Helt, M. Menotti, M. Liscidini, and J. E. Sipe, "Beyond photon pairs—nonlinear quantum photonics in the high-gain regime: a tutorial," Adv. Opt. Photon. **14**, 291–403 (2022).
28. R. J. A. Francis-Jones, T. A. Wright, A. V. Gorbach, and P. J. Mosley, "Engineered photon-pair generation by four-wave mixing in asymmetric coupled waveguides," arXiv, arXiv:1809.10494 (2018).
29. O. F. Anjum, P. Horak, Y. Jung, M. Suzuki, Y. Yamamoto, T. Hasegawa, P. Petropoulos, D. J. Richardson, and F. Parmigiani, "Bandwidth enhancement of inter-modal four wave mixing Bragg scattering by means of dispersion engineering," APL Photonics **4**, 022902 (2019).
30. M. Cordier, A. Orieux, B. Debord, F. Gérome, A. Gorse, M. Chafer, E. Diamanti, P. Delaye, F. Benabid, and I. Zaquine, "Active engineering of four-wave mixing spectral correlations in multiband hollow-core fibers," Opt. Express **27**, 9803–9814 (2019).
31. H. Fukuda, K. Yamada, T. Shoji, M. Takahashi, T. Tsuchizawa, T. Watanabe, J.-I. Takahashi, and S.-I. Itabashi, "Four-wave mixing in silicon wire waveguides," Opt. Express **13**, 4629–4637 (2005).
32. A. Melloni, F. Morichetti, and M. Martinelli, "Four-wave mixing and wavelength conversion in coupled-resonator optical waveguides," J. Opt. Soc. Am. B **25**, C87–C97 (2008).
33. S. M. M. Friis, J. G. Koefoed, K. Guo, and K. Rottwitt, "Analytic description of four-wave mixing in silicon-on-insulator waveguides," J. Opt. Soc. Am. B **35**, 702–710 (2018).
34. S. Signorini, M. Sanna, S. Piccione, M. Ghulinyan, P. Tidemand-Lichtenberg, C. Pedersen, and L. Pavesi, "A silicon source of heralded single photons at 2 μm," APL Photonics **6**, 126103 (2021).
35. B. L. S. Marlow, "Degenerate four-wave-mixing as a low-power source of squeezed light," Opt. Express **28**, 38169–38183 (2020).
36. A. I. Lvovsky, "Squeezed light," in *Photonics: Scientific Foundations, Technology and Applications*, D. L. Andrews, ed. (Wiley, 2015), pp. 121–163.
37. B. Bagchi, R. Ghosh, and A. Khare, "A pedestrian introduction to coherent and squeezed states," Int. J. Mod. Phys. A **35**, 2030011 (2020).
38. L. G. Helt, M. Liscidini, and J. E. Sipe, "How does it scale? Comparing quantum and classical nonlinear optical processes in integrated devices," J. Opt. Soc. Am. B **29**, 2199–2212 (2012).
39. J.-M. Lee, M.-S. Kim, J. T. Ahn, L. Adelmini, D. Fowler, C. Kopp, C. J. Oton, and F. Testa, "Demonstration and fabrication tolerance study of temperature-insensitive silicon-photonic MZI tunable by a metal heater," J. Lightwave Technol. **35**, 4903–4909 (2017).
40. S. Clemmen, K. P. Huy, W. Bogaerts, R. G. Baets, P. Emplit, and S. Massar, "Continuous wave photon pair generation in silicon-on-insulator waveguides and ring resonators," Opt. Express **17**, 16558–16570 (2009).
41. C. Ma and S. Mookherjea, "Prospects for photon-pair generation using silicon microring resonators with two photon absorption and free carrier absorption," OSA Contin. **3**, 1138–1153 (2020).
42. L. G. Helt, Z. Yang, M. Liscidini, and J. E. Sipe, "Spontaneous four-wave mixing in microring resonators," Opt. Lett. **35**, 3006–3008 (2010).
43. Z. Vernon, M. Menotti, C. C. Tison, J. A. Steidle, M. L. Fanto, P. M. Thomas, S. F. Preble, A. M. Smith, P. M. Alsing, M. Liscidini, and J. E. Sipe, "Truly unentangled photon pairs without spectral filtering," Opt. Lett. **42**, 3638–3641 (2017).
44. P. G. Kwiat, A. M. Steinberg, and R. Y. Chiao, "Observation of a "quantum eraser": a revival of coherence in a two-photon interference experiment," Phys. Rev. A **45**, 7729–7739 (1992).
45. C. J. Oton, C. Manganelli, F. Bontempi, M. Fournier, D. Fowler, and C. Kopp, "Silicon photonic waveguide metrology using Mach–Zehnder interferometers," Opt. Express **24**, 6265–6270 (2016).
46. M. A. Popović, C. Manolatou, and M. R. Watts, "Coupling-induced resonance frequency shifts in coupled dielectric multi-cavity filters," Opt. Express **14**, 1208–1222 (2006).
47. W. Bogaerts, P. De Heyn, T. Van Vaerenbergh, K. De Vos, S. Kumar Selvaraja, T. Claes, P. Dumon, P. Bienstman, D. Van Thourhout, and R. Baets, "Silicon microring resonators," Laser Photonics Rev. **6**, 47–73 (2012).
48. A. Prinzen, M. Waldow, and H. Kurz, "Fabrication tolerances of SOI based directional couplers and ring resonators," Opt. Express **21**, 17212–17220 (2013).
49. A. Peruzzo, J. McClean, P. Shadbolt, M.-H. Yung, X.-Q. Zhou, P.-J. Love, A. Aspuru-Guzik, and J. L. O'Brien, "A variational eigenvalue solver on a photonic quantum processor," Nat. Commun. **5**, 4213 (2014).
50. J. Wang, S. Paesani, Y. Ding, R. Santagati, P. Skrzypczyk, A. Salavrakos, J. Tura, R. Augusiak, L. Mančinska, D. Bacco, D. Bonneau, J. W. Silverstone, Q. Gong, A. Acín, K. Rottwitt, L. K. Oxenløwe, J. L. O'Brien, A. Laing, and M. G. Thompson, "Multidimensional quantum entanglement with large-scale integrated optics," Science **360**, 285–291 (2018).
51. S. Aaronson and A. Arkhipov, "The computational complexity of linear optics," arXiv, arXiv:1011.3245 (2010).
52. D. J. Brod, E. F. Galvão, A. Crespi, R. Osellame, N. Spagnolo, and F. Sciarrino, "Photonic implementation of boson sampling: a review," Adv. Photonics **1**, 034001 (2019).
53. G. Dufour, T. Brünner, A. Rodríguez, and A. Buchleitner, "Many-body interference in bosonic dynamics," New J. Phys. **22**, 103006 (2020).
54. M. Pont, R. Albiero, S. E. Thomas, N. Spagnolo, F. Ceccarelli, G. Corrielli, A. Brieussel, N. Somaschi, H. Huet, A. Harouri, A. Lematre, I. Sagnes, N. Belabas, F. Sciarrino, R. Osellame, P. Senellart, and A. Crespi, "Quantifying *n*-photon indistinguishability with a cyclic integrated interferometer," Phys. Rev. X **12**, 031033 (2022).
55. C. Dittel, G. Dufour, M. Walschaers, G. Weihs, A. Buchleitner, and R. Keil, "Totally destructive many-particle interference," Phys. Rev. Lett. **120**, 240404 (2018).
56. J. Münzberg, C. Dittel, M. Lebugle, A. Buchleitner, A. Szameit, G. Weihs, and R. Keil, "Symmetry allows for distinguishability in totally destructive many-particle interference," PRX Quantum **2**, 020326 (2021).
57. C. Dittel, G. Dufour, G. Weihs, and A. Buchleitner, "Wave-particle duality of many-body quantum states," Phys. Rev. X **11**, 031041 (2021).
58. K. Zielnicki, K. Garay-Palmett, D. Cruz-Delgado, H. Cruz-Ramirez, M. F. O'Boyle, B. Fang, V. O. Lorenz, A. B. U'Ren, and P. G.

Kwiat, "Joint spectral characterization of photon-pair sources," J. Mod. Opt. **65**, 1141–1160 (2018).
59. K. Garay-Palmett, H. McGuinness, O. Cohen, J. S. Lundeen, R. Rangel-Rojo, A. B. U'ren, M. G. Raymer, C. J. McKinstrie, S. Radic, and I. A. Walmsley, "Photon pair-state preparation with tailored spectral properties by spontaneous four-wave mixing in photonic-crystal fiber," Opt. Express **15**, 14870–14886 (2007).
60. J. B. Christensen, J. G. Koefoed, K. Rottwitt, and C. J. McKinstrie, "Engineering spectrally unentangled photon pairs from nonlinear microring resonators by pump manipulation," Opt. Lett. **43**, 859–862 (2018).
61. J. C. Adcock, J. Bao, Y. Chi, X. Chen, D. Bacco, Q. Gong, L. K. Oxenløwe, J. Wang, and Y. Ding, "Advances in silicon quantum photonics," IEEE J. Sel. Top. Quantum Electron. **27**, 6700224 (2021).